Meteorologische Zeitschrift, PrePub DOI 10.1127/metz/2016/0777

Numerical simulations of homogeneously nucleated natural cirrus and contrail-cirrus. Part 1: How different are they?

Simon Unterstrasser[1*], Klaus Gierens[1], Ingo Sölch[1] and Martin Lainer[1,2]

[1]Deutsches Zentrum für Luft- und Raumfahrt (DLR) – Institut für Physik der Atmosphäre, Oberpfaffenhofen, Germany
[2]now at: Institute of Applied Physics, University of Bern, Bern, Switzerland

(Manuscript received January 15, 2016; in revised form May 11, 2016; accepted June 17, 2016)

Abstract

The evolution of contrail-cirrus and natural cirrus formed by homogeneous nucleation is studied over up to ten hours by means of a Large-Eddy Simulation (LES) model equipped with a Lagrangian ice microphysics module. This is the first time that both cloud types are investigated in a single study. Characteristics of their life cycles depend strongly on the synoptic scenario. Weak, but enduring updraughts allow for the longest life times of contrail-cirrus. For cirrus clouds, the updraught speed during their formation is most crucial. Once contrails lose their linear shape they are hardly distinguishable from natural cirrus which makes it difficult to evaluate the extent and effect of the anthropogenic cloud modification. Despite their different formation mechanisms (contrails are generated locally and have initially much higher ice crystal number concentrations than natural cirrus) we could not single out microphysical criteria that could help to distinguish in general between both cloud types in observations.

Keywords: Large eddy simulation, Lagrangian ice microphysics, Natural cirrus, contrail cirrus, aviation

1 Introduction

The most important contribution of aviation to anthropogenic climate change is due to formation of contrails that may persist for hours in the atmosphere under favourable conditions. Growing in lateral extent they sometimes cover the local sky. This result has been obtained mostly from climate models that have been retrofitted with modules to describe contrails (e.g. Ponater et al., 2002; Burkhardt and Kärcher, 2009). Alternatively, a combined model-observational approach was employed (Schumann and Graf, 2013).

It would be desirable to corroborate the results of such climate simulations with observations, but airborne measurement campaigns are not able to provide a global perspective and are often biased to the thickest and easiest-to-observe contrails. Nevertheless, aircraft measurement campaigns with the German research aircraft HALO (High Altitude LOng range) like ML-Cirrus, which took place in spring 2014, can supply a wealth of data due to their rich instrumentation (ACP/AMT Special Issue, 2016). This can help to gain a deeper process understanding and to indirectly improve climate estimates.

Measurements from satellites give a global (or at least hemispheric) view (Iwabuchi et al., 2012), but have difficulties to distinguish between contrail-cirrus (old contrails which have lost their initial linear shape) and natural cirrus. They suffer from a similar selection bias because their detection efficiency increases with the optical thickness of the observed contrail or cirrus (Kärcher et al., 2009). Satellite missions like the A-train carry nowadays combinations of active and passive instruments and a synergistic use of these measurements allows retrieving more quantities than before. However, the question arises whether there are microphysical and radiative properties that can be exploited to distinguish between contrail-cirrus and natural cirrus over their whole lifetime. To answer such questions, cloud resolving modelling can help, and additionally, the results of those models can guide measurements in airborne campaigns in order to corroborate or disprove the model predictions.

This paper is intended to make such numerical comparisons between contrail-cirrus and cirrus clouds. We are guided by a number of relevant questions:

- What are the essential differences between contrail-cirrus and cirrus?
- Which differences survive up to the end of their lifetime (or at least up to the end of a simulation)?
- Which processes and properties of the ambient atmosphere are relevant for the emergence of these differences?
- Is it possible to exploit these differences for a distinction of both cloud types in remote sensing, in-situ applications or a synergistic use of various measurement techniques?

There is a vast literature on both cirrus cloud and contrail simulations, but for a rigorous comparison simulations of these clouds in the same atmospheric situation

*Corresponding author: Simon Unterstrasser, DLR Oberpfaffenhofen, 82234 Wessling, Germany, e-mail: simon.unterstrasser@dlr.de

or even together in a single simulation are necessary. However, the latter introduces complications by the interaction between contrail and cirrus and should be only the second step after separate simulations of contrails and cirrus for the same atmospheric background. First, the basic differences resulting from the essentially different formation pathways of contrails and cirrus clouds have to be understood in such situations. Even without the complex interaction between cirrus and embedded contrails too many parameters like meteorological conditions or aircraft properties influence the contrail evolution, that it is well conceivable that a distinct difference found in one situation will not be found or will be insignificant in another one.

Contrail evolution depends sensitively on meteorological parameters like temperature, humidity, vertical wind shear, but also on atmospheric stability, depth of the supersaturated layer in which they are formed, radiation scenario (i.e. position of the sun, ambient cloudiness), and of course on aircraft properties (fuel flow rate, wing span, weight, speed) (Jensen et al., 1998; Unterstrasser and Gierens, 2010a; Unterstrasser and Gierens, 2010b; Lewellen et al., 2014; Lewellen, 2014; Unterstrasser and Görsch, 2014). For cirrus clouds these are vertical wind speed, depth of the supersaturated layer, temperature, pressure, concentration of heterogeneous ice nuclei, stability, radiation scenario, etc. (e.g. Dobbie and Jonas, 2001; Liu et al., 2003; Spichtinger and Gierens, 2009b; Spichtinger and Gierens, 2009a; Jensen et al., 2011; Sölch and Kärcher, 2011). Moreover, contrails usually appear in clusters instead of single isolated objects, at least in regions of intense air traffic, and there is competition for the available water vapour (Gierens, 1998; Unterstrasser and Sölch, 2013). Moreover, cirrus clouds are often found close to contrails and their formation may be suppressed by contrails, diminishing the cirrus cloud coverage (Burkhardt and Kärcher, 2011). Thus, contrail evolution does also depend on whether there are other contrails or cirrus clouds nearby and how close they are.

It would be counterproductive to vary all these parameters in one study because that would render the paper unreadable. Instead we have concentrated on a few important parameters, mainly wind shear (important for the lateral growth of contrails) and vertical wind speed (important for the number of ice crystals nucleated in a homogeneous cirrus nucleation event and the amount of available water vapour). This means, that the list of relevant questions will not be completely answered in this paper, and only first results can be provided. Proceeding on this way will eventually provide insight, being helpful in several directions. On the one hand, reliable recipes for observation and measuring strategies may be identified that are able to distinguish contrail-cirrus from natural cirrus on a global scale. On the other hand, the findings can help to advance contrail parametrisations in global scale models (Burkhardt and Kärcher, 2009; Rap et al., 2010; Schumann, 2012).

To simplify the description of our simulation results we refer to cirrus if we speak of a naturally formed cirrus. The term "contrail" refers both to linear contrails and aged contrails where the term contrail-cirrus would be more appropriate. Conveniently, this circumvents the need to distinguish between contrail and contrail-cirrus. The neutral term ice cloud is used, if the cloud type is unspecified.

Section 2 presents the methodology and introduces the employed model and the design of the numerical set-up. Section 3 juxtaposes the evolution of contrail and of cirrus and highlights the most prominent differences. The results are discussed in Section 4 and conclusions are drawn in Section 5.

2 Methods

In this section, the employed model with its numerical set-up is introduced and properties that will be used in the later analysis are defined.

2.1 Model description

The numerical simulations have been carried out with the non-hydrostatic anelastic model EULAG (Smolarkiewicz and Margolin, 1997) which employs the positive definite advection scheme MPDATA (Smolarkiewicz and Margolin, 1998) in its Eulerian operation mode. A microphysical module using Lagrangian tracking of ice crystals (Sölch and Kärcher, 2010) is fully coupled to EULAG and forms the version EULAG-LCM. With this model version the simulation of both natural cirrus and contrails is possible. Recent examples are studies of a mid-latitude cirrus cloud system with special focus on aggregation (Sölch and Kärcher, 2011) and the contrail evolution during the vortex phase (Unterstrasser, 2014; Unterstrasser and Görsch, 2014).

The microphysical module LCM uses an explicit representation of size-resolved non-equilibrium aerosol and ice microphysics. Ice crystals are represented in the model by Lagrangian simulation particles (SIPs). Every SIP represents a large number of ice crystals with identical properties, and the actual number of SIPs as well as the number of ice crystals a SIP represents vary dynamically during a run of the model. In particular, a SIP splitting technique (Unterstrasser and Sölch, 2014) is applied to ensure sufficiently high SIP concentrations in the diluting contrails. In its complete form the LCM comprises non-equilibrium growth of liquid supercooled aerosol particles, their homogeneous freezing, heterogeneous nucleation of ice nuclei in the deposition or immersion mode, growth of ice crystals by deposition of water vapour, their gravitational sedimentation, aggregation between ice crystals due to differential sedimentation, turbulent dispersion of ice crystals, latent heat release, and radiative impact on particle growth. Nucleation of ice is sub-cycled and the nucleation time step is usually smaller than the dynamical time step. Not all of above mentioned processes are

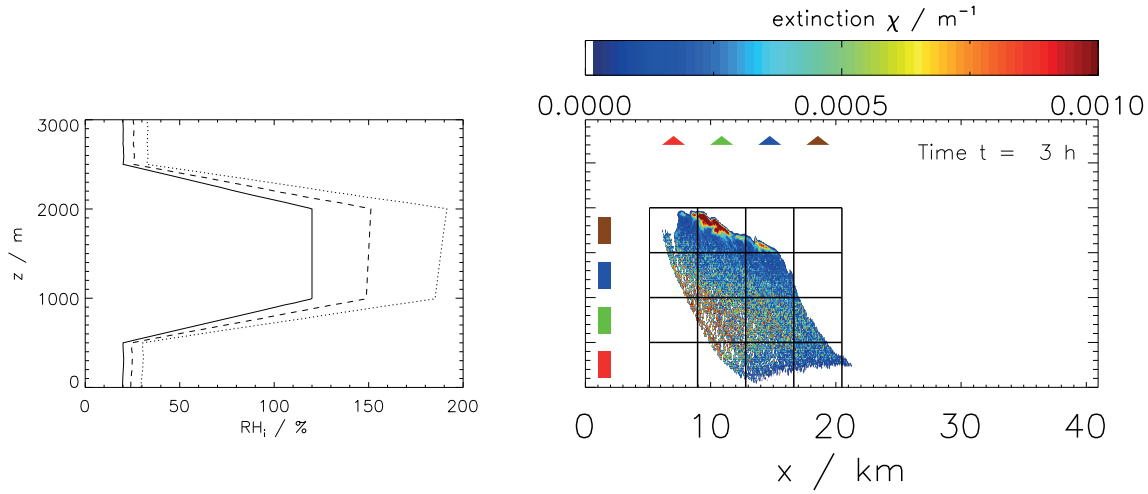

Figure 1: Left: Vertical profile of relative humidity RH_i in the beginning (solid) and after an adiabatic temperature decrease by 2 K (dashed) and 4 K (dotted), respectively. The thickness of the ice supersaturated layer increases from 1200 m to 1380 m or 1550 m. The flight altitude of the contrail-producing aircraft is at $z_{CA} = 2000$ m. The temperature at cruise altitude $T_{CA} = T(z_{CA}) = 217$ K. Right: Snapshot of the extinction coefficient χ of an exemplary contrail-cirrus after 3 h. The overlaid grid illustrates the divisions used in Figure 11.

switched on in the present simulations in order to reduce the complexity of the situations. For the sake of simplicity, heterogeneous nucleation, aggregation and radiation are deactivated, although they can strongly alter the evolution of natural and contrail-cirrus (e.g. Liu et al., 2003; Spichtinger and Gierens, 2009a; Unterstrasser and Gierens, 2010b; Sölch and Kärcher, 2011; Lewellen, 2014).

Several types of crystal habits are included via habit-dependent mass-size and mass-area relationships which enter the expressions for microphysical and radiative quantities (capacitance, fall speed, extinction cross-section). A priori, a specific habit type has to be selected as the model is not yet capable of predicting the habit evolution. In this study, hexagonal columns are chosen for both the contrail and cirrus simulations. Possible differences in the habit characteristics between contrails and cirrus are not considered in the simulation and analysis.

The information contained in the SIPs is mapped on the Eulerian grid, which is used for all non-ice variables. Then, e.g., the ice water content at each grid point is computed by summing up the ice mass represented by each SIP belonging to this grid box and dividing this sum by the grid box volume.

The subgrid turbulence model uses the TKE-approach. Synoptic scale updraught motion is prescribed via an external forcing term in the temperature equation in order to accommodate for the adiabatic temperature change. Details of the implementation can be found in Unterstrasser and Gierens (2010b).

2.2 Simulation set-up

The simulation set-up for the present study follows that of the recent simulations of contrail-cirrus with EULAG-LCM (Unterstrasser, 2014; Unterstrasser and Görsch, 2014). A 2D model, the domain of which is perpendicular to flight direction and represents some portion of the UT/LS (upper tropospheric/lower stratospheric) region, is used. In the vertical direction (coordinate z), the domain dimension is 3 km. In the horizontal direction (coordinate x), the domain dimension can be as large as 80 km. In the (vertical) middle of the domain an ice-supersaturated layer of 1 km thickness and initial relative humidity (with respect to ice) of 120 % is prescribed (see Figure 1 left). Figure 1 right depicts a typical aged contrail that is tilted due to vertical wind shear and that has developed a fall streak penetrating into the subsaturated layer beneath.

The total simulation time ranges between 6 h and 10 h. The dynamical time step is 2 s or 1.25 s depending on vertical wind shear. The nucleation time step ranges from 0.1 s to 0.5 s depending on the updraught speed w_{syn}.

Synoptic scale updraughts with various intensities ranging from $w_{syn} = 1\,\mathrm{cm\,s^{-1}}$ to $20\,\mathrm{cm\,s^{-1}}$ are prescribed. The final adiabatic cooling is either 2 K or 4 K and corresponds to an uplift of roughly 200 m or 400 m, respectively. This implies shorter updraught periods for larger w_{syn}. In further scenarios, no updraught or a weak downdraught with $w_{syn} = -1\,\mathrm{cm\,s^{-1}}$ is prescribed. Table 1 summarises the updraught velocities and periods of the various scenarios. The temporal evolution of the background relative humidity $RH_i^*(t)$ at $z = 2000$ m is shown in Figure 2.

The various updraught scenarios are associated with different synoptic situations. Slow updraught is found in prefrontal zones, a region where large decks of contrail-cirrus have been observed (Haywood et al., 2009; Laken et al., 2012). Stronger updraught occurs due to gravity waves. Note that the strong updraught scenario used in this study does not correspond to a full wave cycle as the downdraught phase is neglected.

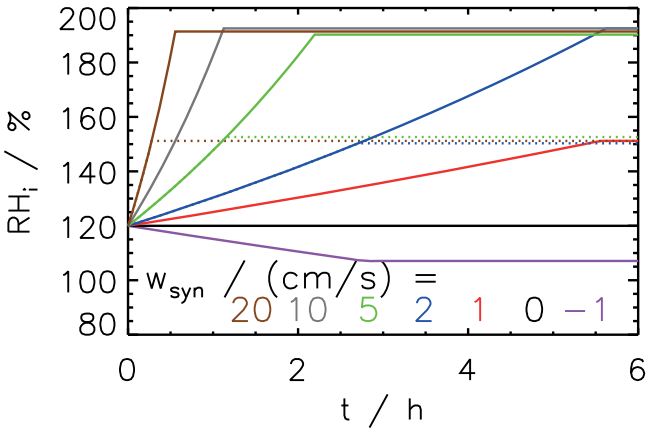

Figure 2: Temporal evolution of relative humidity $RH_i^*(t)$ at z = 2000 m for various w_{syn} (as indicated in the legend or given in Table 1). The final adiabatic cooling is 2 K (dotted) or 4 K (solid).

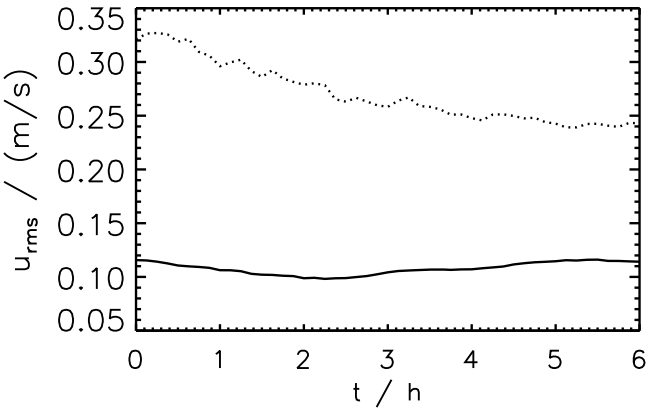

Figure 3: Temporal evolution of the root mean square of the turbulent velocity fluctuations given by $\hat{u} = \left[\sum_i \left(u_i^2 + w_i^2\right)\right]^{0.5}$. The sum is taken over all grid boxes. The solid curve depicts the default case, the dotted one the case with stronger turbulence.

Table 1: Characteristics of the various updraught scenarios: updraught speed w_{syn}, approx. time of cirrus formation t_{nuc}. The length of the updraught period t_{updr} is given in the third/fifth column and the final hypothetical relative humidity $RH_{i,f}$ is given in the fourth/sixth column ("1" or "2" stands for the 4 K and 2 K-case, respectively). The rightmost column indicates the colours used in several plots throughout the paper.

w_{syn} in cm/s	t_{nuc} in s	t_{updr1} in s	$RH_{i,f1}$ in %	t_{updr2} in s	$RH_{i,f2}$ in %	colour
−1	–	10000	107			magenta
0	–	–	120			black
1	–	20000	150			red
2	10200	20000	190	10000	150	blue
5	4000	8000	190	4000	150	green
10	2000	4000	190	–	–	grey
20	1000	2000	190	1000	150	brown

The atmosphere is assumed to be stably stratified with a Brunt-Väisälä frequency $N_{BV} = 10^{-2}\,s^{-1}$, a typical value for the upper troposphere. Background turbulent velocity fields were produced by a-priori simulations and have a root mean square (rms) value $\hat{u} = \left[\sum_i \left(u_i^2 + w_i^2\right)\right]^{0.5} \approx 0.1\,m\,s^{-1}$. The temporal evolution of $\hat{u}$ is displayed in Figure 3. Although the rms-value is supposed to decay slowly over time, as no "forced turbulence"-mechanism is included, in the displayed case $\hat{u}$ even increases after 3 hours, probably due to latent heating effects.

Homogeneous nucleation is initiated preferentially at the top of the supersaturated layer where the nucleation threshold humidity of $RH_{crit} \approx 155\,\%$ is surpassed first (see Figure 2). Cirrus formation starts at different points in times t_{nuc} in the various scenarios (see Table 1).

Three kinds of simulations are performed:

- simulation of a contrail only (referred to as CONTRAIL simulation)
- simulation of natural cirrus only (referred to as CIRRUS simulation)
- simulation of a contrail interacting with natural cirrus (referred to as INTERACTION simulation)

At $t = 0$, all CONTRAIL and INTERACTION simulations are initialised with the same 5 minute old contrail that is about 500 m deep and 200 m broad and contains about $\mathcal{N}_0 = 1.7 \cdot 10^{12}$ ice crystals per meter of flight path. This corresponds to a an ice crystal 'emission' index of $2.8 \cdot 10^{14}$(kg fuel)$^{-1}$ and roughly half of the ice crystals surviving the vortex phase (Unterstrasser, 2014). Data of a 3D vortex phase simulation with EULAG-LCM (Unterstrasser, 2014) are incorporated into the present simulation domain (see Figure 15 in the latter reference for an illustration). For this, the 3D-fields (e.g. perturbations of water vapour concentration q_v and potential temperature θ) are averaged along flight direction, interpolated on the coarser grid and embedded into the enlarged 2D model domain. SIPs with similar positions (neglecting the coordinate y along flight direction) and ice crystal sizes are merged in order to reduce their overall number.

Around 10^6 SIPs represent the contrail-cirrus, which was shown to be sufficient for most analyses of such simulations (Unterstrasser and Sölch, 2014). Producing robust probability density functions (as shown in Figure 8) requires higher SIP numbers and thus a SIP splitting technique is applied in selected simulations (see Section 3.1 and 4.1 in Unterstrasser and Sölch, 2014).

The cruise altitude of the contrail generating aircraft is z_{CA} = 2000 m (above the bottom of the domain). The temperature at cruise altitude is T_{CA} = 217 K, a typical value of the extra-tropical upper troposphere. The only difference between the CONTRAIL simulation and the INTERACTION simulation is that homogeneous nucleation is switched off or on. For the CIRRUS cases, the simulation domain is initially void of ice crystals and the domain width is reduced to 10 km to reduce computing costs. Up to $5 \cdot 10^6$ SIPs are generated to resolve the highly non-linear ice nucleation process. The stochastic

Table 2: Differences between natural cirrus clouds and contrails (incl. contrail cirrus).

Cirrus formed by homogeneous nucleation	Contrail
Formation	
needs considerable supersaturation	is possible even in completely dry air, persistence requires at least ice saturation
Ice crystal number	
proportional to $w_{syn}^{3/2}$	depends on aircraft and meteorological properties
depends on temperature	
Ostwald ripening rarely occurs	Ostwald ripening occurs
Ice crystal size	
ice crystal size mode growing with time, $\gg 10\,\mu m$	ice crystal size mode hardly growing with time, $\approx 10\,\mu m$
close to monomodal size distribution	two modes possible (core and fall streak)
In-cloud relative humidity	
frequently $RH_i \gg 100\%$	$RH_i \approx 100\%$ in the core frequently $RH_i \gg 100\%$ in the fall streaks
Lifetime	
longer for higher updraught speed	longer for longer updraught duration

nucleation implementation and a SIP merging technique as described in Unterstrasser and Sölch (2014) are employed.

For the sake of completeness, INTERACTION simulations have been introduced here, even though their presentation and discussion is deferred to PART2 (Unterstrasser et al., 2016).

2.3 Definitions

Let us first introduce several quantities. Some of them are motivated by analysing the contrail evolution. Nevertheless, most definitions are also meaningful for a cirrus cloud.

The total extinction E of a contrail is the horizontal integral of the extinction $1 - e^{-\tau(x)}$, where $\tau(x)$ is the optical thickness along the vertical direction.

$$E = \int (1 - e^{-\tau})\, dx \approx \int \tau\, dx = \tilde{\tau} \times \tilde{B} \qquad (2.1)$$

$\tau(x)$ is given by $\int \chi dz$, where χ is the extinction coefficient. Total extinction measures the disturbance of the shortwave radiative flux. For small τ-values the approximation holds and E can be interpreted as product of characteristic optical thickness $\tilde{\tau}$ and width $\tilde{B}$ and comprises information about microphysical and geometric properties. Details can be found in Unterstrasser and Gierens (2010a, see their Eq. 12). This quantity cannot be directly translated into a (solar) radiative forcing. This requires further knowledge on the incident radiation fluxes which depend inter alia on solar zenith angle, surface albedo or the presence of underlying water clouds (Forster et al., 2012).

The definition of a width B_{OD} of a contrail considers its visibility by a human observer. It takes into account all contrail columns with τ larger than 0.02, which is roughly the visibility threshold.

The mean optical thickness τ_m is the average of τ over all contrail columns with $\tau \geq \tau_c = 0.005$.

The mean ice crystal concentration n_{mean} is the average of n over all contrail parts with $n \geq 10^2\ \mathrm{m}^{-3}$.

Following Yang et al. (2000, their Eq. 13), the effective ice crystal diameter of the total cloud is given by

$$D_{eff} = \frac{3 \sum_i V_i}{2 \sum_i A_i}, \qquad (2.2)$$

where i runs over all SIPs of the domain. V_i is the total volume of all ice crystals in SIP i and A_i is the total projected area of the hexagonal crystals in SIP i.

The ice crystal size distributions are given in terms of L, where L is the maximum size of ice crystals.

The computation of L and A_i is based on mass-size and mass-area relations of Mitchell (1996) for hexagonal columns.

3 Comparison of contrail with cirrus evolution

As we are seeking differences between contrails and cirrus clouds, we start with their essentially different formation mechanisms (see Table 2) and consider the question how initially different properties are transferred to later stages of the evolution.

If the environment is cold enough (Schumann, 1996), contrail formation occurs in a confined area behind an aircraft and the ice crystals get redistributed by the trailing wake vortices during the first few minutes. The number of ice crystals produced in the cooling exhaust plume and surviving the vortex phase depends on fuel, combustion, aircraft and meteorological parameters (e.g. Kärcher and Yu, 2009; Unterstrasser and Görsch, 2014; Unterstrasser, 2016). The present

simulations start with about 20 cm^{-3} on average and locally up to 200 cm^{-3} ice crystals in the 5 minute old contrail.

Cirrus crystals form whenever and wherever the relative humidity surpasses a certain threshold, well above the saturation level (depending on the temperature or ice forming properties of the background ice nuclei) and their number depends strongly on the vertical wind speed, if we focus on homogeneous nucleation only.

This leads to two characteristic differences, in terms of geometry and microphysics:

1. Young contrails are small scale clouds that spread and get diluted over time, whereas the cirrus spatial scales are determined by the humidity field.

2. The ice crystal number concentrations rarely exceed 10 cm^{-3} in cirrus (Krämer et al., 2009) while it typically ranges from 10^4 cm^{-3} to 10^5 cm^{-3} in freshly generated contrails (Schröder et al., 2000). The strong dilution during the jet and vortex phase (Schumann et al., 1998; Unterstrasser et al., 2014) and crystal loss during the latter of the two phases (Sussmann and Gierens, 1999) reduce contrail crystal concentrations substantially.

In contrast to the crystal concentration the ice mass concentration is for both, the contrail and cirrus, rather determined by the ambient conditions (absolute humidity and vapour mass in excess of ice saturation). The differences resulting from ice mass concentrations are thus expected to be less important.

In the following, results of the simulations of cirrus and contrails are presented and it is investigated whether significant differences between both cloud types remain for a while. We begin with juxtaposing the evolution of cirrus and contrails for various "synoptic" scenarios (speed and duration of updraught, wind shear); Subsections 3.1 and 3.2 focus on basic properties of and fundamental differences between cirrus and contrails, respectively. In Subsection 3.3, a refined comparison between both cloud types follows.

3.1 Cirrus

Simulations of cirrus are carried out up to 10 h, with w_{syn} = 2 cm s^{-1}, 5 cm s^{-1}, 10 cm s^{-1} and 20 cm s^{-1}. The initial relative humidity in the moist layer is 120 % and the uplift is stopped once the layer is adiabatically cooled by 4 K. As a consequence of the fixed total adiabatic cooling, the amount of excess vapour (the vapour that is available for deposition on ice crystals) is eventually equal in all simulations.

Figure 4 compiles various cirrus properties: total extinction, effective diameter as well as the total number and mean concentration of ice crystals. The faster the air layer rises, the earlier RH_i crosses the nucleation threshold and cirrus ice crystals form. Most notably is the strong dependence of total ice crystal number $\mathcal{N}$ on the updraught speed w_{syn}. More ice crystals nucleate for higher w_{syn}.

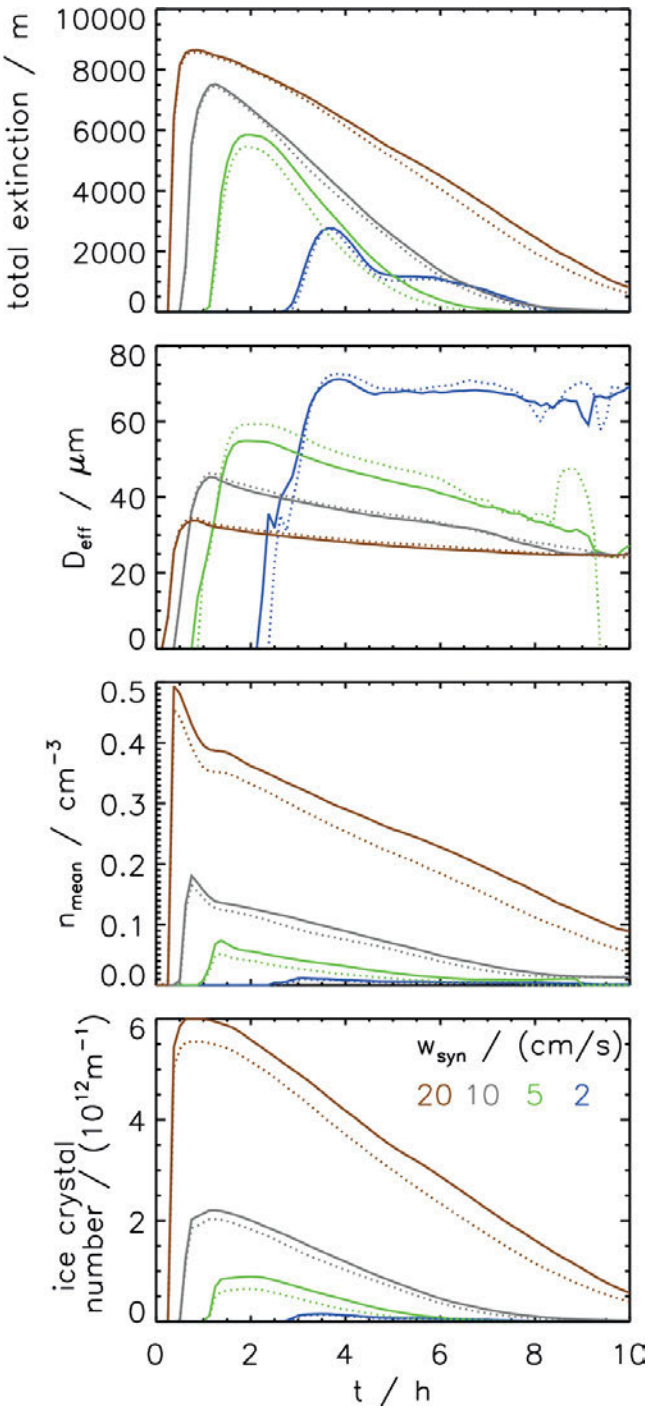

Figure 4: Temporal evolution of several cirrus properties for various synoptic scenarios (colour coding for w_{syn} see Table 1 or legend in bottom panel): total extinction E, effective diameter D_{eff} as well as the mean ice crystal number concentration and the total ice crystal number (from top to bottom). The low shear cases are denoted with solid lines, the high shear cases with dotted lines. Colour coding for w_{syn}, see Table 1. The final adiabatic cooling ΔT_{cool} is 4 K in any case.

This $\mathcal{N}$-variation has major implications. The crystals are smaller for higher w_{syn} and the effective diameters reach maximum values between 30 µm and 70 µm

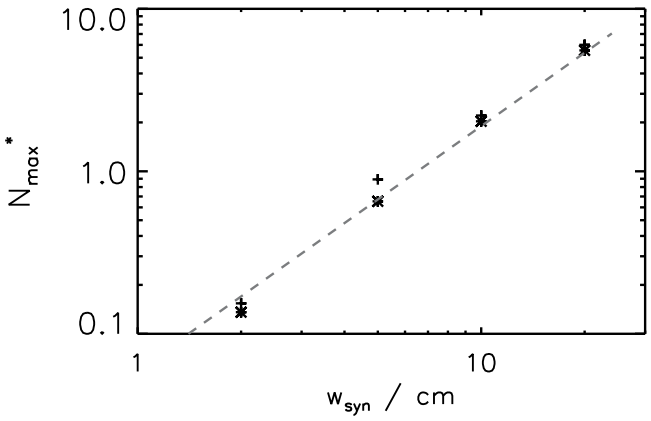

Figure 5: Relationship between updraught speed w_{syn} and maximum normalised total ice crystal number $\mathcal{N}^*_{max}$ of a cirrus cloud. $\mathcal{N}^*_{max} = \max_t(\mathcal{N})/\mathcal{N}_{scal}$ where $\mathcal{N}_{scal}$ is an arbitrarily chosen scaling factor. The two types of symbols show the low and high wind shear cases. The dashed line shows the analytic approximation $\propto {w_{syn}}^{1.5}$ following Kärcher and Lohmann (2002).

(see second row of Figure 4). This implies a higher total extinction for the same ice mass and a longer life time as sedimentation fluxes are smaller. After ten hours only the cirrus at $w_{syn} = 20\,\mathrm{cm\,s^{-1}}$, although emerging as the first one, has a non-negligible total extinction (see first row of Figure 4) because it consists of the smallest crystals. Figure 5 shows a $\mathcal{N}_{max} \sim {w_{syn}}^{1.5}$ relationship (where the maximum of $\mathcal{N}$ is taken over time). This is in accord with earlier analytical estimates by Kärcher and Lohmann (2002) who related ice crystal concentrations n to w_{syn}. The excellent agreement between both approaches is somewhat surprising as the simulation takes into account several process not accounted for in the analytical approach. For instance, 1.) the total crystal number $\mathcal{N}$ is used here instead of some typical crystal concentration and 2.) the effect of sedimentation is considered. Moreover, turbulent motions enhance ice crystal formation due to the non-linear character of nucleation. In particular for small w_{syn}, this effect can be strong as the turbulent fluctuations represent the major contribution to the actual updraught speeds. A sensitivity study with stronger turbulence ($\hat{u} = 0.32\,\mathrm{m\,s^{-1}}$) pronounces the enhancement and shows a weaker dependence of $\mathcal{N}_{max}$ on w_{syn}. The exponent of the fit function is then around 1.2 (not shown).

A fairly weak impact of vertical wind shear s on cirrus properties is found. Slightly fewer ice crystals form for higher vertical wind shear (see bottom row of Figure 4). A similar tendency was found in Spichtinger and Gierens (2009b). Note, however, that in our set-up the moist layer and with it the cirrus extends horizontally throughout the whole domain. The effect of shear may be larger in situations with a less uniform or laterally confined moist layer.

3.2 Contrail

In this section the contrail evolution up to 6 hours in the absence of cirrus formation is discussed. For this, homogeneous nucleation is switched off. Uplift scenarios as in the CIRRUS simulations (with adiabatic cooling of 4 K) and additional cases with $w_{syn} = 1, 0$, and $1\,\mathrm{cm\,s^{-1}}$ are considered. The ambient relative humidity of the latter cases evolves as shown by the red, black, and magenta curves in Figure 2. Note that in the case $w_{syn} = -1\,\mathrm{cm\,s^{-1}}$ the downdraught is stopped before the moist layer gets subsaturated.

Figure 6 displays the evolution of characteristic contrail properties, viz. total extinction, mean optical thickness, mean number concentration and geometric width, over simulation time. It shows results of simulations with low (left) and high (right) wind shear s. The evolution of crystal number and effective diameter, which do not depend strongly on s, are displayed in Figure 7 for the low wind shear cases only.

In the downdraught scenario (magenta lines) the contrail evolves differently from all other cases and this exceptional case is discussed first. A much stronger loss of ice crystals and a lower total extinction compared to the $w_{syn} \geq 0\,\mathrm{cm\,s^{-1}}$-cases can be observed. The contrail soon becomes faint. The optical thickness takes values around the visibility threshold and the contrail width starts to decrease after two hours as an increasing portion of the contrail becomes sub-visual or vanishes completely. It is noteworthy that a contrail can survive for quite a while (not just minutes) in (slowly) subsiding areas, albeit as a faint specimen.

The remainder of this section focuses on the climatically more relevant cases with $w_{syn} \geq 0\,\mathrm{cm\,s^{-1}}$ (Duda et al., 2009). Generally, the contrails are initially narrow and spread over time. The contrail width B_{OD} increases with time, roughly in a linear fashion. Depending strongly on vertical wind shear s, B_{OD} attains values of 20 km for $s = 0.002\,\mathrm{s^{-1}}$ and 60 km for $s = 0.006\,\mathrm{s^{-1}}$. This is in line with width values for contrails up to one hour age retrieved by scanning lidar (Freudenthaler et al., 1995).

There are three sources of excess water vapour that deposits on contrail ice crystals:

1. entrainment of fresh supersaturated air through the contrail borders, mainly in horizontal direction
2. the decrease of the saturation pressure due to adiabatic cooling in the contrail's interior, and
3. the moist layer below for ice crystals falling into it.

The relevance of the entrainment mechanism increases with wind shear, that of the cooling mechanism with uplift speed and that of the sedimentation mechanism with the thickness of the ice supersaturated layer. Inside the contrail, high ice crystal number concentrations imply a short deposition time scale. The available water vapour gets quickly converted into ice and relative humidity is close to saturation.

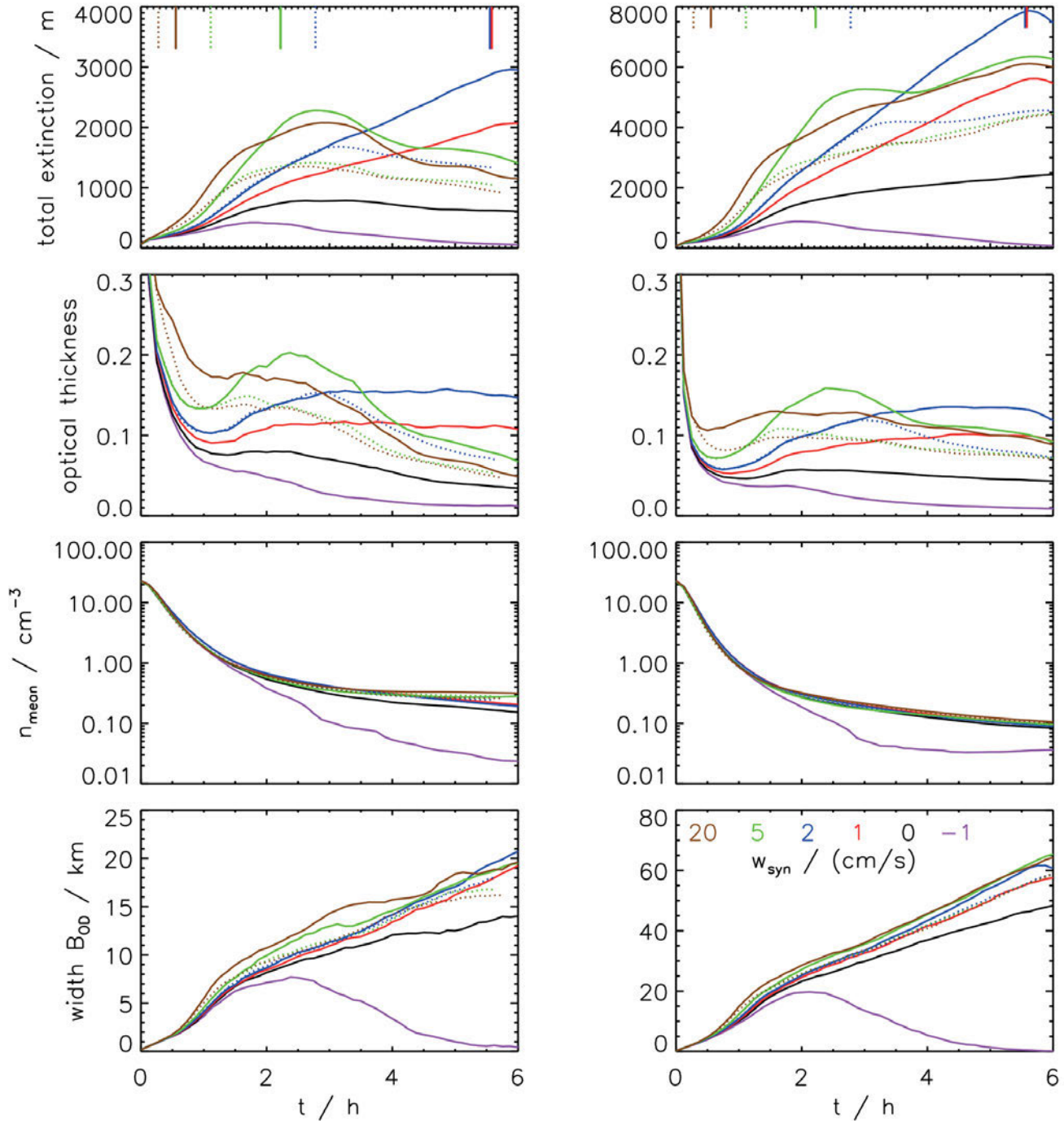

Figure 6: Temporal evolution of several contrail properties for various synoptic scenarios (colour coding for w_{syn} see Table 1 or legend in bottom right panel): total extinction E, mean optical thickness τ_m, mean number concentration and width B_{OD} (from top to bottom). The left panel shows the low shear case ($s = 0.002\,\mathrm{s}^{-1}$), the right one the high shear case ($s = 0.006\,\mathrm{s}^{-1}$). Solid lines: standard scenarios; dotted lines: shorter updraught period (resulting ΔT_{cool} is 2 K). The vertical bars in the top panels indicate the times the updraughts comes to a halt.

Let us first consider the low wind shear cases (left column of Figure 6). Over the first two to three hours the ice mass (not shown) and total extinction grow with time. The growth rate increases with w_{syn}. At some reversal point in time, total extinction starts to decrease as sedimentation losses are no longer balanced by depositional growth. In the simulations, this occurs after the updraught comes to a halt. If the updraught is strong, but short, ice crystals quickly grow in the beginning. But soon sedimentation leads to a substantial loss of ice mass and after six hours the total extinction is well below its peak value. Contrails seem to be most long-living in an environment with slow, but steady updraught (blue and red solid lines). In these cases, the total extinction grows over the whole simulation period of six hours.

Mean optical thickness values, τ_m, decrease from about 1 in the beginning to < 0.2 after an hour, as the contrails get tilted. Subsequently, τ_m may increase for a

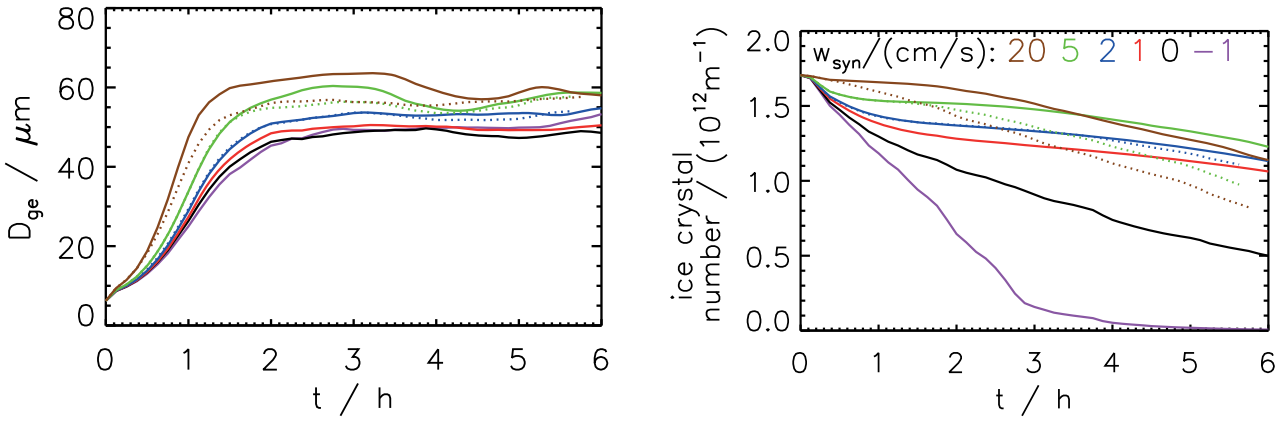

Figure 7: Analogous to Figure 6, but only simulations with low wind shear are shown, as the high wind shear results are similar. The displayed quantities are effective diameter D_{eff} and total ice crystal number for various updraught speeds w_{syn} (colour coding see Table 1 or legend in right panel).

while, however starts to drop again, once the updraught motion stops. The vertical bars in Figure 6 mark the end of the updraught in the various cases and clearly show the coincidence with the onset of the τ_m-decrease. Contrails facing a slow, but steady updraught are eventually the optically thickest. This may explain the formation of very long living contrails as observed by Minnis et al. (1998), Duda et al. (2004), Haywood et al. (2009) and Laken et al. (2012).

The number of ice crystals is steadily decreasing in all contrails. Notably, ice crystals are lost by two different effects. The obvious one is that ice crystals fall into the dry layer below and sublimate there. However, ice crystals are also lost inside the originally moist layer once relative humidity approaches 100 %. The latter is enhanced by Ostwald ripening, which is a spectral broadening of the ice crystal size distribution due to the Kelvin effect (Lewellen, 2012). Lewellen et al. (2014) coined the term "in-situ loss" for this effect. The relative importance of the two mechanisms depends on the environmental conditions and a closer inspection is deferred to Section 3.3.4. In combination, there is a non-linear and non-monotonic relation between w_{syn} and the ice crystal number at the end of the simulations.

In a high-wind-shear environment, the contrail evolution is in many aspects similar to the low-wind-shear case. Thus it suffices to point out the apparent differences: 1.) Optical thickness has moderately lower values. Generally, τ_m seems to depend more sensitively on w_{syn}. 2.) Total extinction attains larger values, as the contrails become broader and cover a larger area. 3.) Total extinction increases over a longer period. The entrainment of fresh supersaturated air is stronger and sedimentation losses are balanced over a longer period.

The evolution of total ice crystal number and effective diameter of the ice crystals are similar for both values of wind shear. Thus, Figure 7 shows only the low-wind-shear results. The effective diameters increase within the first two hours (see left panel). After this initial growth period they remain nearly constant at about 50 µm to 60 µm. Interestingly, the final value is fairly insensitive to the uplift speed. The observed pattern is similar to the one in a preceding study on contrail-cirrus produced by different aircraft (Unterstrasser and Görsch, 2014). A more detailed discussion of spatially-resolved effective diameters is deferred to Section 3.3.1. The mean ice crystal number concentrations (see right panel) drop strongly over time due to dilution and the formation of a fallstreak both increasing the contrail area. Compared to this aging effect, the shear-induced differences in n_{mean} appear to be of secondary importance.

In the cases with $w_{syn} \geq 2\,\mathrm{cm\,s^{-1}}$ and $\Delta T_{cool} = 4\,\mathrm{K}$ (as used for the CIRRUS simulations), RH_i increases to 190 % outside of the contrail and suppression of homogeneous nucleation is actually not realistic. As the contrail growth by entrainment may thus be overestimated, simulations with $\Delta T_{cool} = 2\,\mathrm{K}$ and $RH_{i,final} \approx 150\,\%$ are added. In these scenarios it is more plausible that cirrus formation has not yet started (dotted lines in Figs. 2, 6 and 7). All statements made above remain valid for the 2 K cases.

3.3 Detailed Comparison

3.3.1 Crystal sizes and number concentrations

Figure 8 shows histograms (PDFs) of ice crystal concentrations n for three cloud ages (t = 0.5 h, 2 h and 4.5 h). Contrail PDFs are shown for low and high vertical wind shear, cirrus PDFs for low and high updraught speed, as these parameters presumably have the largest impact on n.

The cirrus PDFs have one pronounced peak depending w_{syn}; at around $0.1\,\mathrm{cm^{-3}}$–$1\,\mathrm{cm^{-3}}$ for $20\,\mathrm{cm\,s^{-1}}$ and $0.001\,\mathrm{cm^{-3}}$–$0.01\,\mathrm{cm^{-3}}$ for $2\,\mathrm{cm\,s^{-1}}$. Over time a tail with smaller concentration values emerges. The simulated concentrations cover a large range ($< 10^{-5}$–$1\,\mathrm{cm^{-3}}$) similar to what large observational data sets reveal

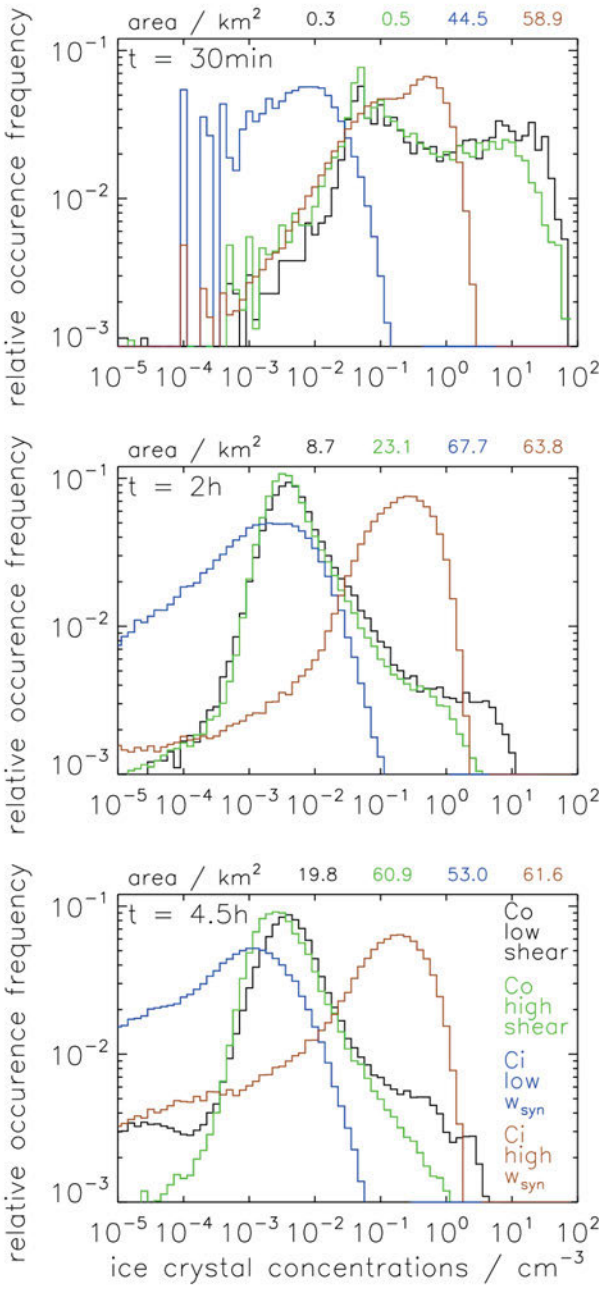

Figure 8: Relative occurrence frequency of ice crystal number concentrations in 30 min, 2 h and 4.5 h old cirrus or contrails. Contrail at weak and high wind shear (black: $s = 0.002\,\mathrm{s}^{-1}$; green: $s = 0.006\,\mathrm{s}^{-1}$); cirrus at low and high updraught speed (blue: $w_{syn} = 2\,\mathrm{cm\,s}^{-1}$; brown: $w_{syn} = 20\,\mathrm{cm\,s}^{-1}$). Note that here the indicated times refer to the age of the cloud, not to the simulated time as, e.g., in Figure 10. On top of each panel, the extent of the sampling area for each specific cloud is documented.

(Krämer et al., 2009; Luebke et al., 2013). The maximum observed values are larger than our simulated ones. Those may have been measured when the real updraught speeds exceeded our maximum value of $20\,\mathrm{cm\,s}^{-1}$ or when the measured cirrus was "polluted" by contrails (as already pointed out by Ström and Ohlsson, 1998).

In contrast to the cirrus PDFs, the contrail PDFs have two distinct peaks after half an hour. Concentrations of 10 cm^{-3}–100 cm^{-3} are found in the contrail core (right peak). Such concentrations have been often measured in contrail cores of this age (Heymsfield et al., 1998; Poellot et al., 1999; Schröder et al., 2000; Febvre et al., 2009). The left peak at around 0.01 cm^{-3}–0.1 cm^{-3} represents the developing fall streak and compares well to measurements of the contrail periphery in Heymsfield et al. (1998).

After 2 hours the fall streak of the contrail becomes mature and the most likely concentrations shift to 0.001 cm^{-3}–0.01 cm^{-3} (comparable to the values in a 'low updraught' cirrus). The right peak representing the contrail core becomes less pronounced over time. On the one hand, the maximum concentrations drop due to dilution. High shear accelerates this process. On the other hand, the relative frequency drops. This is simply due to the fact, that the fall streak covers a larger and larger area and the relative fraction of the contrail core area decreases. The concentrations in the contrail core are similar to those in a high updraught cirrus.

These results indicate that aged contrails may be identified as such only if the updraught speed is low and the contrail core is sampled. As in-situ measurements are the preferred observation method to determine number concentrations, questions arise, how likely the core of a contrail is hit and sampled.

Compared to the PDFs of number concentrations, PDFs of ice mass concentrations or intermediate moments (i.e. total length or total surface area) show smaller differences between cirrus and contrails (not shown) as ice mass is more strongly influenced by ambient humidity conditions.

Consider now Figs. 9 and 10 for the analysis of ice crystal size distributions (SD). Here, the size L refers to the maximum dimension of an ice crystal in any direction.

Driven by the high number concentrations, any initial supersaturation in a contrail core is quickly reduced and the ice crystals grow to approximately 10 µm size (as confirmed by several measurements: Heymsfield et al., 1998; Poellot et al., 1999). They cease growing in the same moment when the uplift stops. Thus, in a contrail core there are small ice crystals at an approximately ice saturated state, which favours the occurrence of Ostwald ripening, an effect that manifests itself in the SDs as a sublimation tail (see Figure 9 bottom). In contrast, there is less competition for excess vapour in a cirrus and individual cirrus crystals can grow over a much longer period, even beyond the point the uplift stops. They attain much larger sizes than contrail crystals (except for contrail fall streaks). The predominance of large crystals excludes Ostwald ripening in cirrus clouds in most cases (see Figure 10).

The contrail fall streaks consist of the largest ice crystals with maximum sizes of about 300 µm (Figure 9 top). Note that simulations with $\Delta T_{cool} = 2\,\mathrm{K}$ are displayed, as $\Delta T_{cool} = 4\,\mathrm{K}$-simulations may overestimate

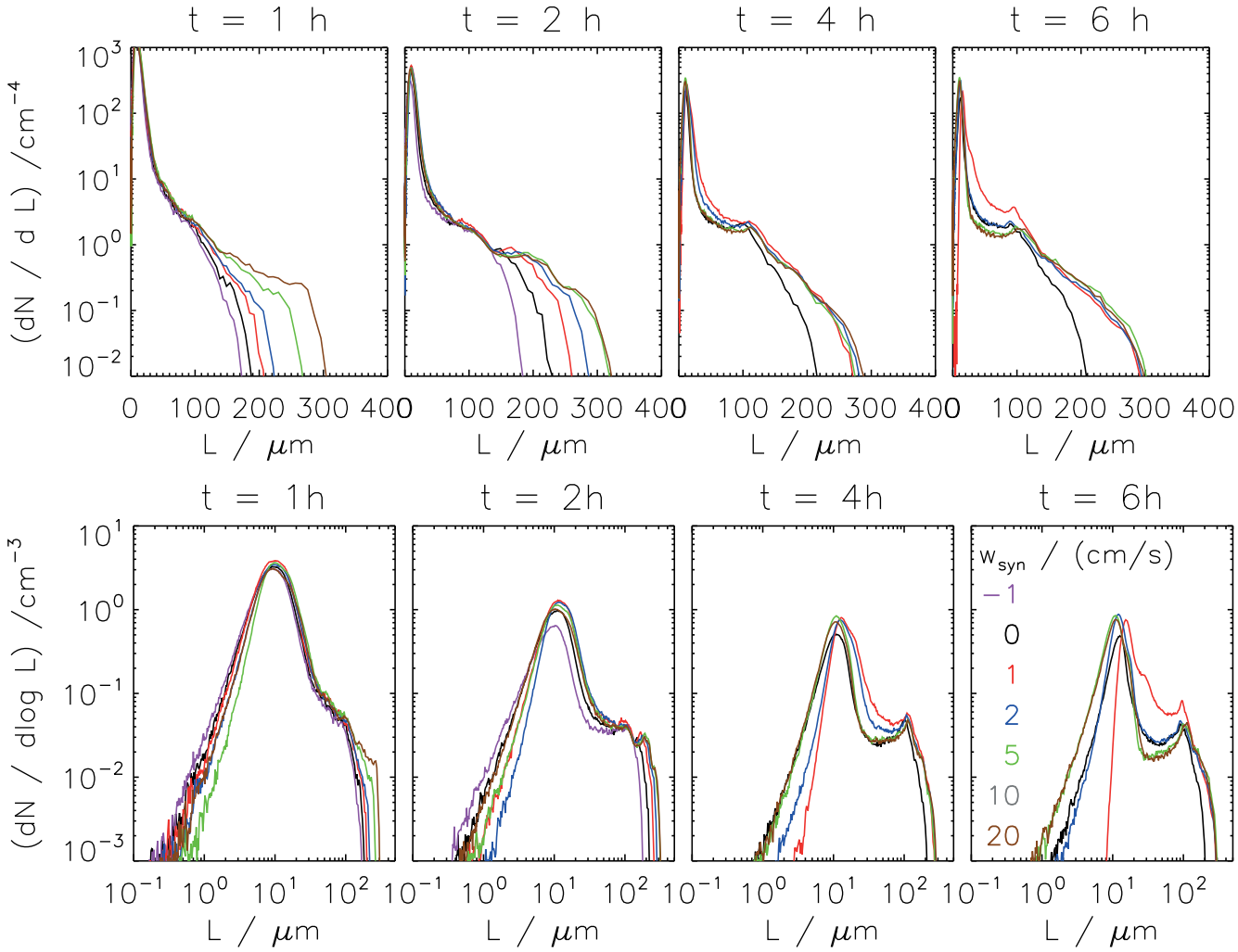

Figure 9: Contrail ice crystal size distributions for various contrail ages (see label on top) and updraught speeds w_{syn} (colour coding see Table 1 or legend in bottom right panel). The top row shows the SD on linear scale, the bottom row on a log scale. The vertical wind shear is $s = 0.002\,\mathrm{s}^{-1}$. The updraught period is chosen such that ΔT_{cool} is at most 2 K.

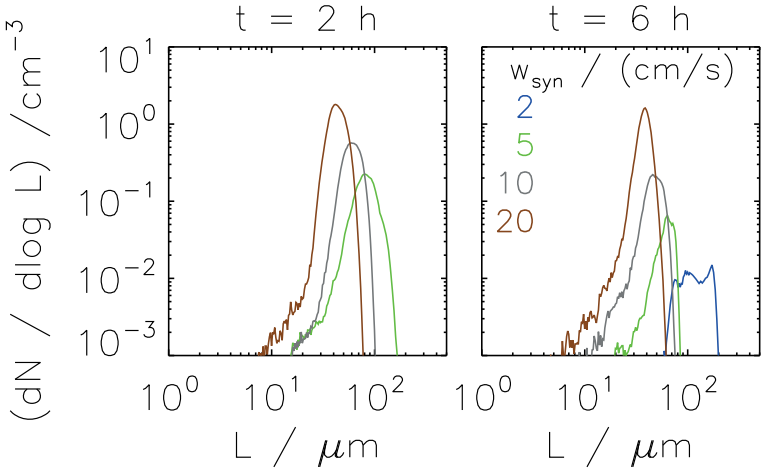

Figure 10: Cirrus ice crystal size distributions for various times (see label on top) and updraught speeds w_{syn} (colour coding see Table 1 or legend in right panel). The vertical wind shear is $s = 0.002\,\mathrm{s}^{-1}$.

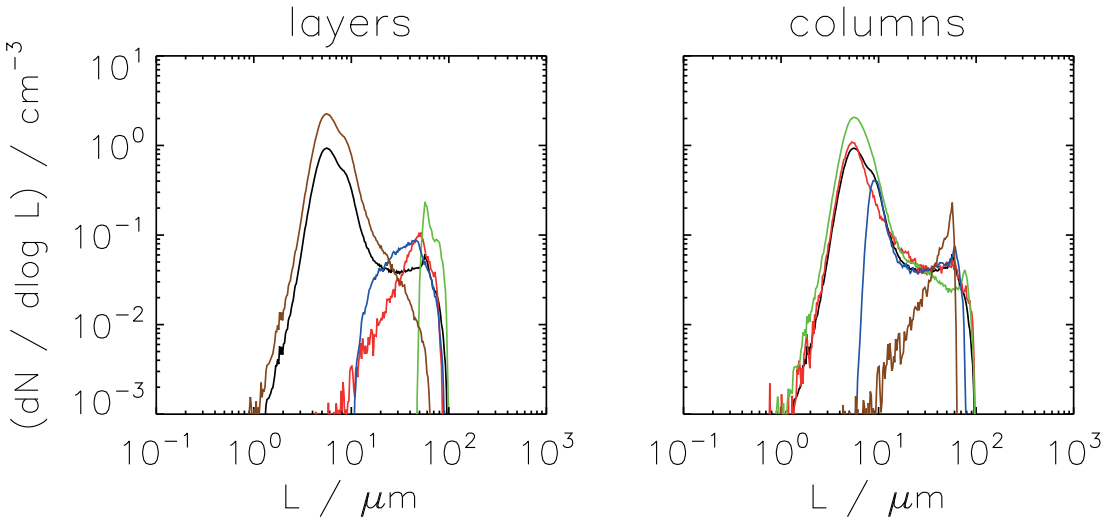

Figure 11: Spatial dependence of size distributions in a 3 h old contrail. The contrail is separated into four 500 m thick layers (left) or four 3.8 km broad columns (right). The sub-domains and the colour coding are depicted in Figure 1 right. The black curves show the size distribution of the total contrail as already shown in Figure 9. Depicted is the case with $w_{syn} = 5\,\mathrm{cm\,s^{-1}}$ and $s = 0.002\,\mathrm{s^{-1}}$.

the entrainment and crystal growth at the contrail borders. Such large contrail crystals were also observed during the SUCCESS measurement campaign (Lawson et al., 1998).

Occasionally, a second mode at about 100 µm appears in the SDs. The mechanism behind this may be best explained by an inspection of height-resolved SDs depicted in Figure 11 left. This second mode is an accumulation mode produced from two effects, namely the growth of ice crystals falling from the contrail core through the supersaturated layer (reaching maximum sizes larger than the second mode) and the sublimation below the supersaturated layer. That is, the second mode appears because it is populated from both sides, from smaller growing crystals in the moist layer (blue to green curve) and from larger sublimating crystals in the dry layer underneath (green to red curve). Moreover, Figure 11 left shows that crystal sizes below 10 µm only appear in the top 500 m of a contrail (brown curve).

In the simulated cirrus SDs, no second mode is evident. Furthermore, the maximum crystal sizes are smaller than those of the contrails. But this result cannot be generalised, as the maximum sizes in contrails can be smaller, when the formation of the fall streak is inhibited (due to a reduced depth of the moist layer or a cirrus forming below the contrail, Unterstrasser et al., 2016). Moreover with aggregation switched off, the formation of very large crystals (exceeding mm size) and of a second mode in cirrus size distributions (Mitchell et al., 1996; Ivanova et al., 2001; Sölch and Kärcher, 2010) may be suppressed in our simulations. The effect of aggregation in contrail-cirrus has not been studied so far and is a topic of future research. The modal sizes of cirrus ice crystals depend, as expected, on w_{syn} and range from 40 µm to more than 100 µm. In any case, the sizes are larger than those found in a contrail core.

Measuring high concentrations of small ($\lesssim$ 10 µm) crystals may thus be a robust indication for a contrail and can be exploited in the analysis of in-situ data. However, at lower flight altitudes with higher temperatures and/or for reduced soot emissions the mean sizes of the small particle mode can be higher (Unterstrasser and Gierens, 2010a; Unterstrasser and Gierens, 2010b; Lewellen, 2014). In a sensitivity study, which we call "factor 10"-experiment, the initial ice crystal number is reduced by a factor of 10, but still most crystals are smaller than 20 µm (not shown). Experience from previous simulations tells that the effect of a temperature variation (covering the most common flight altitudes) is lower than that seen in the "factor 10"-experiment. However, for temperatures around 230 K (just below the threshold for contrail formation), much fewer ice crystals nucleate initially (Kärcher et al., 1998) and the modal sizes may exceed the 20 µm-limit.

As discussed above, the heterogeneity of contrails in vertical direction (discussed in terms of SDs, see Figure 11 left) is linked to the effect of sedimentation. Yet, contrails are also heterogeneous in horizontal (i.e. transverse) direction (Figure 11 right) due to their localised formation and subsequent spreading, even for homogeneous background conditions as prescribed in the simulations. In particular, high concentrations of small crystals are only found in columns where the contrail core is located. This generally demonstrates that in-situ measurements with an incomplete sampling of the contrail system must be interpreted with care.

The effective diameter D_{eff} can be derived from satellite measurements (Nakajima and King, 1990; Bugliaro et al., 2011). The retrieved values may be representative of the cloud top only though (Platnick, 2000). It turned out that in the presented simulations the maximum effective diameters in cirrus depend on

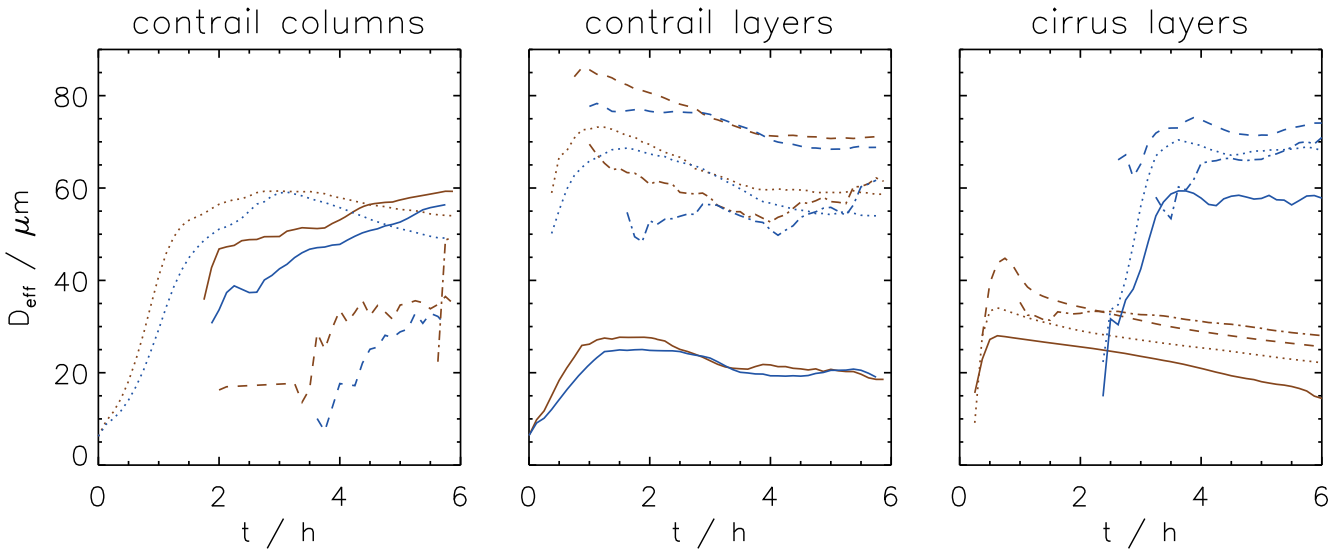

Figure 12: Spatial dependence of effective diameters D_{eff} in contrails (left and middle) and cirrus (right) for w_{syn} = 2 cm s^{-1} (blue) and 20 cm s^{-1} (brown). The domain is separated into four 10 km broad columns (left) or four 500 m thick layers (middle and right). The line styles of the sub-domains are solid, dotted, dashed, dash-dotted from left to right or from top to bottom, respectively.

updraught speeds (maximum values of 30 µm–70 µm) whereas in contrails D_{eff} reaches values of 50 µm–60 µm irrespective of w_{syn}. These are D_{eff}-values averaged over the whole cloud, which is rather coarse, as a contrail or cirrus usually covers several pixels of a satellite image. Therefore, it is useful to evaluate D_{eff} for distinct segments of the cirrus and contrails (Figure 12) similar to the SDs in Figure 11. Again, there is a strong dependence on horizontal contrail location (left panel), while the cirrus is fairly homogeneous in horizontal direction (not shown). The contrail D_{eff}-values depend also strongly on altitude and are fairly insensitive to updraught speed. In the contrail top, D_{eff} is around 20 µm and in the fall streaks around 50 µm–80 µm. Cirrus ice crystal nucleation occurs throughout a deep supersaturated layer and D_{eff}-values increase slightly with decreasing altitude. Unlike contrails, cirrus effective diameters depend strongly on updraught speed. In the sublimation layer (dash-dotted curves), D_{eff} decreases. Common to all simulations is the pattern of an initial growth period followed by a period of quasi-constant values, as already seen for the D_{eff} averaged over the whole cloud.

In the model, the contrail effective diameters are within the range of cirrus effective diameters. Thus, the simulations imply that D_{eff}-measurements alone are in general not sufficient to distinguish between cirrus and contrails. If strong updraughts can be ruled out, small D_{eff}-values hint at the presence of contrails. However, we want to mention two caveats of this conclusion. Satellite retrievals usually employ an inversion technique that degrades for small crystal sizes and optical thickness. Hence, the determination of D_{eff} in particular in contrail cores is associated with larger errors.

In the model, D_{eff} is given by Eq. 2.2. Interpreting D_{eff} as a radiative property of an ice cloud, one implicitly assumes a constant extinction cross-section Q_{ext} = 2 (McFarquhar and Heymsfield, 1998; Mitchell, 2002). This neglects Q_{ext}-variations in the Mie-regime (van de Hulst, 1981) which could be of relevance for the smallest ice crystals in a contrail (Schumann et al., 2011; Baum et al., 2005).

3.3.2 In-cloud relative humidity

In this section, RH_i inside the clouds is evaluated, i.e. all grid boxes with $n > 0$ are considered in the following. Figure 13 shows PDFs of in-cloud RH_i for cirrus (bottom) and contrail (top) for three different cloud ages. In the latter case, the scenarios with ΔT_{cool} = 2 K, which corresponds to a maximum background RH_i^* of around 155 %, are evaluated. In 1 hour old contrails, RH_i is in most parts close to saturation consistent with analytic estimates and in-situ measurements (Kaufmann et al., 2014). Nevertheless, there are also high supersaturation values reaching RH_i^*. These occur in the entrainment area and in the fall streaks. After 4 hours, the high supersaturation in these areas is reduced to well below the background humidity. After 8 hours, virtually all values between 80 % and 150 % occur; values < 100 % appear in the lowermost dry layer. The PDFs of the various w_{syn}-cases are qualitatively similar.

The bottom row shows the corresponding data for cirrus. For a strong, but short updraught (brown curve) RH_i is close to saturation for all displayed times (30 min, 1 h and 2 h). For smaller w_{syn}, supersaturation is maintained over a longer period. For w_{syn} = 2 cm s^{-1}, values around 110 % are most likely after two hours. In a few spots, RH_i is close to the nucleation threshold and nucleation is still on-going.

Many cirrus observations and simulations support the existence of in-cloud supersaturation (Ovarlez et al., 2002; Haag et al., 2003; Gao et al., 2004; Spichtinger

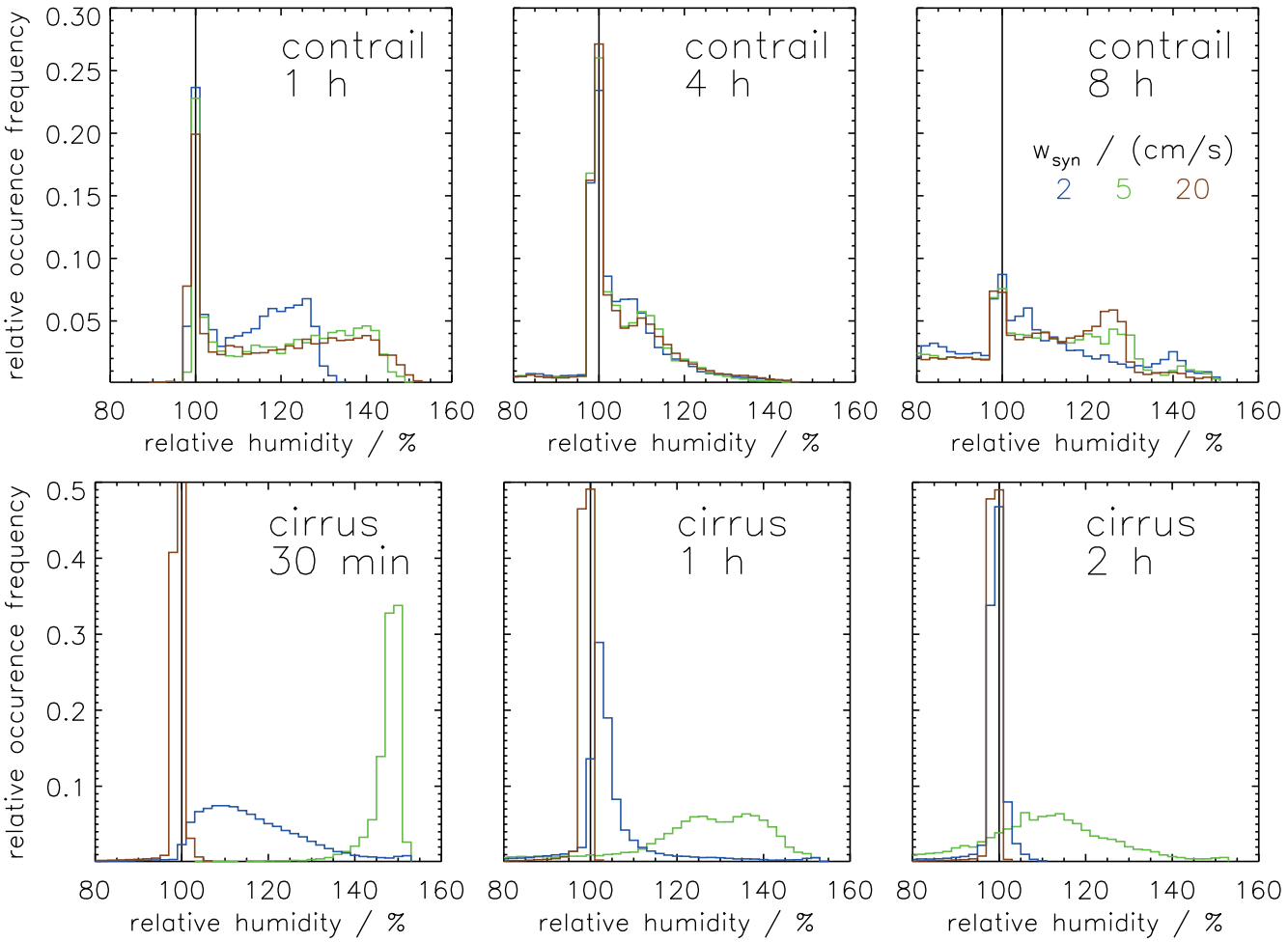

Figure 13: Relative occurrence frequency of in-cloud relative humidity for various cloud ages (see label in each panel) and updraught speeds w_{syn} (colour coding see Table 1 or legend in top right panel). Note that here the indicated times refer to the age of the cloud, not to the simulated time as, e.g., in Figure 10. In the top row contrail cases with low shear $s = 0.002\,\mathrm{s}^{-1}$ and final cooling $\Delta T_{cool} = 2\,\mathrm{K}$ are shown; in the bottom row cirrus cases. Only grid boxes with non-zero ice crystal number concentration are considered. The black vertical line highlights $RH_i = 100\,\%$.

et al., 2004; Krämer et al., 2009; Diao et al., 2014), which may be even more frequent in clouds formed by heterogeneous nucleation (Gierens, 2003; Kärcher et al., 2006), which is not treated in our study.

3.3.3 Turbulence

Next, the impact of the turbulence realisation and intensity on the contrail and cirrus evolution is studied. Simulations with a higher turbulence intensity use a background turbulent velocity field U' with a higher rms value $\hat{u} = 0.32\,\mathrm{m\,s}^{-1}$ instead of the default value $0.1\,\mathrm{m\,s}^{-1}$ (see Figure 3). Moreover, for each selected scenario four simulations with different turbulence realisations of U' are performed. Technically this is done by an horizontal shift of the initial contrail position within the simulation domain. For the cirrus simulations, which run on a 10 km domain, four different slices are extracted from U' of the a-priori simulation, which uses a 40 km domain. The global statistical properties of U' are unchanged for the different realisations of U'.

Figure 14 shows the contrail total extinction for two scenarios ($w_{syn} = 1$ and $20\,\mathrm{cm\,s}^{-1}$) and the cirrus total extinction for one scenario ($w_{syn} = 2\,\mathrm{cm\,s}^{-1}$). In general, the contrail evolution seems to be more strongly affected by the turbulence realisation, whereas the cirrus evolution depends more sensitively on the turbulence intensity.

Apparently, the cirrus formation starts earlier in the strong turbulence case. Stronger vertical motions induce larger RH_i-deviations from the mean state and nucleation is triggered about one hour earlier compared to the default case.

Moreover, more ice crystals form, raising the total extinction. Note that this turbulence enhancement of ice crystal generation is strongest in the depicted slow uplift case. Its relative importance decreases with increasing w_{syn} (not shown). The cirrus evolution depends only weakly on the turbulence realisation (at least for the weakly turbulent default case examined here).

Contrail evolution is also affected by a variation of the turbulence intensity, however to a smaller extent

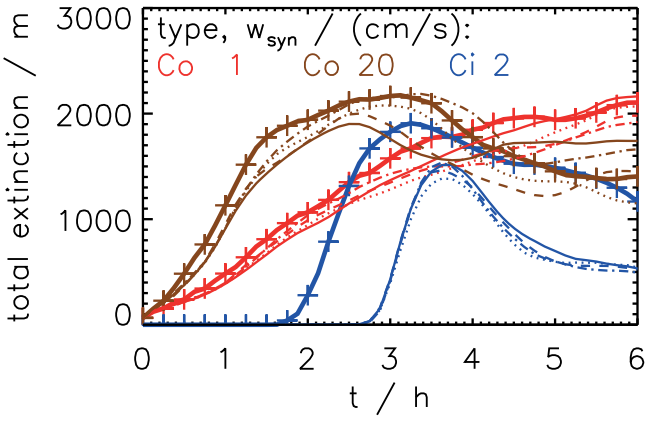

Figure 14: Temporal evolution of total extinction E for two selected contrail scenarios (brown and red) with $\Delta T_{cool} = 4\,\mathrm{K}$ and $s = 0.002\,\mathrm{s}^{-1}$. One scenario is displayed for the cirrus simulations (blue; the values are scaled with a factor of 0.5 to fit into the plot). Colour coding for w_{syn} given in Table 1 or in the legend. For each scenario, four simulations with different turbulence realisations are displayed. Additionally, simulations with stronger turbulence are shown (thicker lines with plus signs).

than the cirrus evolution. Clearly, stronger turbulence leads to a quicker contrail diffusion which leads to a faster increase of total extinction during the first few hours. However, turbulence induced contrail diffusion is just one of several processes contributing to contrail spreading and the situation becomes more intricate after around 3 hours. By then, wind shear has tilted the contrail core and has stretched it laterally. Ice crystals perpetually fall out of the core into supersaturated air and form a strong fall streak as depicted in Figure 1. This combined shear/sedimentation effect becomes more important with time and the contrail spreading becomes less dependent on contrail diffusion and turbulence intensity.

Testing various turbulence realisations, one might expect that young and localised contrails are most susceptible to changes in the exact flow pattern and that differences in the contrail properties are the largest in the beginning. This is clearly not the case. Rather, the contrail evolution becomes more chaotic after around 2–3 hours such that the output of individual simulation runs have to be interpreted implicitly acknowledging that it represents a single sample from an ensemble of possible developments under otherwise equal conditions. In particular for $w_{syn} = 20\,\mathrm{cm\,s^{-1}}$ (brown curves), phases of increasing and decreasing total extinction alternate in an unpredictable fashion. A closer inspection of the simulations reveals that at later times portions of ice crystals fall out from the core randomly and it is not predictable when and where this leads to the formation of new strong bands within the fall streak. This late-time randomness may be even larger in heterogeneous conditions with more patchy fields of relative humidity.

Due to our 2D-approach, our simulations may overestimate the importance of the turbulence realisation, though. Simulating more than just one slice along flight direction may average out some differences and reduce the spread of the model results. Lewellen et al. (2014) finds that full 3D simulations show a smaller spread than quasi-3D simulations where the downstream extent of the model domain was reduced.

3.3.4 Crystal loss

As already noted, ice crystals in contrails are lost by two different mechanisms. Figure 15 details the fractions of ice crystals that are lost by sedimentation (green) or in-situ (blue). In the 'no updraught' case (panel 1a) a large fraction of ice crystals is lost, mainly in-situ. Sedimentation plays a minor role (for the number, not for the mass budget).

Even in slowly ascending air masses, in-situ loss occurs. After around two hours, ice crystals are not lost in-situ any longer and sedimentation takes over. In the strong updraught case (panel 1c), in-situ loss is small in the beginning and sedimentation loss sets in quickly. Dehydration in combination with an interrupted ascent favours the shrinking of crystals in the aged contrail, which then sublimate in-situ. With higher wind shear (panel 2a), contrails spread faster and crystals grow larger. Thus there is stronger sedimentation, which is approximately balanced by less in-situ loss.

Figure 16 details the importance of the Kelvin effect on the extent of in-situ loss and the implications on contrail total extinction and effective diameter. In our model, a Kelvin correction factor $\omega = \exp(a_k/r)$ enters the ice mass growth equation and accounts for the increase of saturation vapour pressure over the curved surface of small ice crystals. r is the radius of the ice crystals, which are assumed to be spherical here. a_k is a parameter that depends inter alia on the surface tension σ for a water vapour-ice interface (see Eq. 5 in Lewellen, 2012, for a definition). So far, a_k was around $2.3 \cdot 10^{-9}\,\mathrm{m}$ in all simulations. Small ice crystals are not perfect spheres with uniform curvature which is one source of uncertainty in the current implementation of the Kelvin correction. The shape assumption is less critical for large crystals, as ω anyway tends to 1 for large r and the correction term vanishes. To account for the uncertainty, simulations with doubled and halved a_k (blue and green curves, respectively) and omitted Kelvin correction (red curves) are performed. As in the top row of Figure 15, scenarios with various w_{syn} are analysed. The black curves depict the simulations with the default a_k-value and are equal to those already shown in Figure 15. The smaller a_k is chosen, the fewer ice crystals are lost. Even in the case with the Kelvin effect omitted, ice crystals can be lost in-situ loss, as seen in the top right and left panel, where the red dashed lines are below 1. This demonstrates that Ostwald ripening enhances sublimation, but is not the only cause as turbulence-induced fluctuations around ice saturation similarly lead to a broadening of the size distribution (Kärcher et al., 2014) and to loss of ice crystals. In the scenario with $w_{syn} = 2\,\mathrm{cm\,s^{-1}}$ (middle panel), where the uplift prevails over

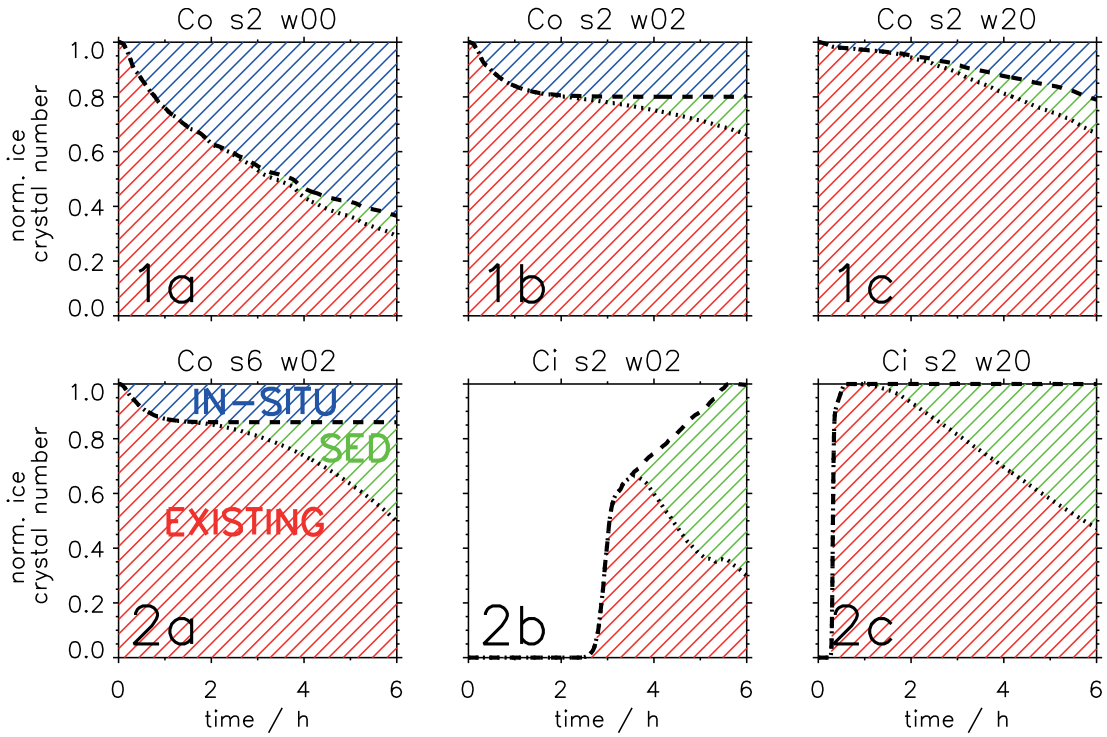

Figure 15: Ice crystal number loss in contrails and cirrus. The red area shows the fraction of existing ice crystals, the green area the fraction lost due to sedimentation and the blue area the fraction lost in-situ (see also labels in bottom left panel). The numbers are normalised by the initial number (contrail cases) or the total number of generated ice crystals (cirrus cases). Panels 1a–1c show contrail cases with low shear and various w_{syn}, panel 1d a high wind shear contrail case. Panels 2a and 2b same conditions as 1a and 1b, but with switched off Kelvin effect. Panels 2c and 2d show cirrus cases with weak and strong updraught.

the total simulated period and water vapour becomes constantly available, ice crystals are lost in-situ only if the Kelvin effect is included.

The Kelvin effect more or less introduces a cut-off filter in the sense that ICs with sizes below a certain threshold are eventually driven to sublimate. Changing or switching off the Kelvin correction in the model affects only the left tail of the ice crystal size distribution, whereas the evolution of the larger ice crystals remains unaffected. Consequently, sedimentation losses are unaffected by such a variation, i.e. the differences between the dashed and dotted lines are the same in each panel. Moreover, total extinction and effective diameter are barely affected. The contribution of the smallest ice crystals is anyway small, such that it makes no difference whether or not they are lost in-situ. Hence, it can be concluded that the uncertainties in the Kelvin effect implementation have a negligible effect on most contrail properties. Neglecting this effect, as usually done in bulk microphysical approaches, which cannot explicitly simulate the spectral broadening, seems acceptable.

Unlike to contrails, in-situ loss does not happen in the cirrus simulations as the ice crystals are too large to be affected by the Kelvin effect. Hence, only sedimentation effectively reduces the crystal number (panel 2b and 2c in Figure 15). In the slow updraught case (panel 2b), there is permanent ice crystal production over the whole simulation period. Nevertheless, ice crystal number drops, once production is outweighed by sedimentation losses.

3.3.5 Lifetimes and radiative effects

The different formation mechanisms lead to contrasting contrail vs. cirrus lifetimes as well. For a cirrus there is the following causal chain: strong uplift → many small ice crystals → slow growth → slow sedimentation → long lifetime, *and vice versa*. In contrast, the corresponding causal chain for contrails is: strong uplift → strong crystal growth → strong sedimentation → short lifetime, *and vice versa* for slow but positive uplift.

The deposition time scale in a contrail core is very small (minutes or shorter, see Khvorostyanov and Sassen, 1998, Table 1), thus the crystals cease to grow as soon as an uplifting motion stops or even reverses. The duration of the uplift has thus a stronger influence on the lifetime of a contrail than its strength. A contrail with weak but steady uplift lives longer than its counterpart in a strong but short updraught.

In a cirrus there can be much larger deposition time scales such that further growth of ice crystals is to some degree decoupled from the vertical motion; the duration of an uplift thus affects cirrus properties less strongly than the updraught speed.

The definition of a width is less meaningful for a cirrus than for a contrail, where the width is the horizontal extent perpendicular to the flight direction. Wind shear (normal to the flight direction) changes the width of these clouds, but in relative terms this effect is much stronger for a narrow object like a contrail than for an already wide object like a cirrus. This implies that total ex-

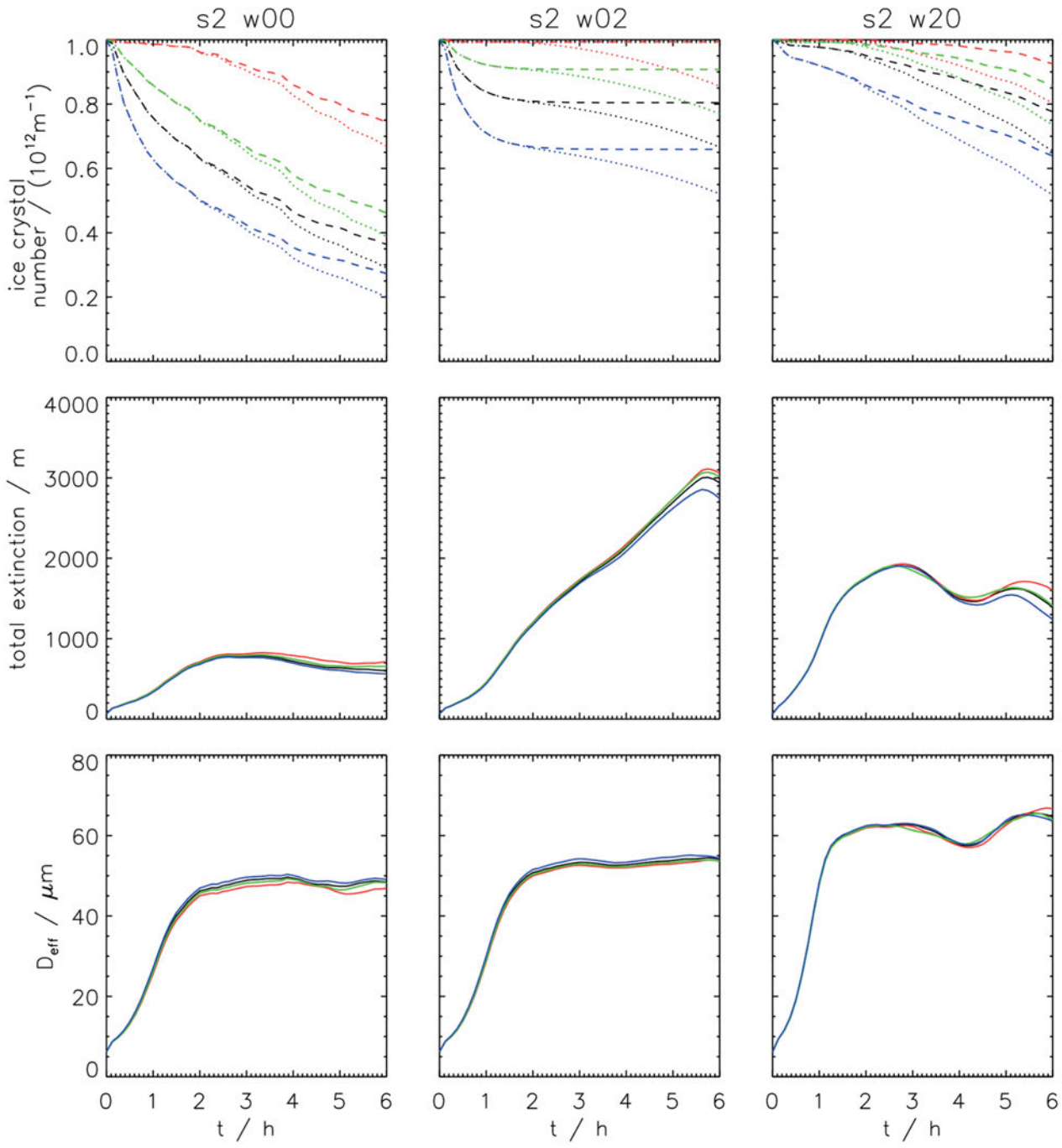

Figure 16: Importance of the Kelvin effect on the contrail evolution. Normalised ice crystal number, total extinction and effective diameter are depicted for various implementations of the Kelvin effect (colours; Kelvin effect switched off (red), $a_k/2$ (green), default a_k (black) and $a_k * 2$ (blue)) and updraught scenarios (panels). In the top panel, the depicted quantities are similar to Figure 15; the dotted line shows the ice crystal number, the difference between the dashed and dotted line represents the fraction of ice crystals lost by sedimentation, and the difference between the dashed line and 1.0 shows the fraction of ice crystals lost in-situ.

tinction of a contrail is sensitive to wind shear while the total extinction of a cirrus is less so and depends more strongly on the horizontal extent of supersaturated layer. In our simulations, the cirrus total extinction scales with horizontal domain size. The optical thickness is proportional to ice water path IWP. The cirrus will always fill the moist layer and thus its IWP is close to the maximum possible. For a contrail, its geometrical depth depends on the flight altitude relative to the bottom of the moist layer; a contrail embedded in a cirrus cloud can have an IWP much smaller than that of the cirrus. This effect on the optical thickness is partly compensated (or over-compensated) by the small effective size of the ice crystals in the contrail core. The optical thickness of both contrails and cirrus clouds increase with the updraught speed, but that of cirrus clouds is more sensi-

tive to the vertical motion (more crystals and more excess moisture) than that of contrails (merely more excess moisture).

4 Discussion

4.1 Model aspects

Our previous work (Unterstrasser and Gierens, 2010a; Unterstrasser and Gierens, 2010b) that focused on contrail-to-cirrus transition relied on a two moment bulk scheme. We investigated the importance of temperature, relative humidity, vertical wind shear and several other parameters in scenarios with time-constant background RH_i. Comparing LCM simulations with $w_{syn} = 0\,\mathrm{cm\,s^{-1}}$ with our previous BULK simulations, it is found that integrated contrail properties like total extinction, ice crystal number and mass agree qualitatively well (Lainer, 2012). In-situ loss cannot be simulated with the BULK model, as only size-resolved microphysics allows the explicit simulation of the Ostwald ripening. Nevertheless, the total ice crystal number evolution is similar, as in the BULK model a numerical artefact (Gierens and Bretl, 2009), which we called turbulent sublimation, leads to crystal loss of about the same magnitude. Several other aspects are more plausibly treated in the LCM approach than in Eulerian approaches, e.g. sedimentation (Wacker and Seifert, 2001; Milbrandt and McTaggart-Cowan, 2010). The low numerical diffusion in LCM leads to less smooth ice microphysical fields that have more fine-scale structures than the BULK results (cf. e.g. Figure 1 with Figure 1 of Unterstrasser and Gierens, 2010a). Both aspects (spectral resolution + Lagrangian advection) give a sound basis to carry out in-depth microphysical analysis (e.g. PDFs of number concentrations, evolution of size distributions).

Some models for contrail-cirrus include mechanisms to sustain turbulence in order to keep its strength at the initial level. In our simulations, no "forced turbulence"-mechanism is taken into account. Rather, the contrail spreading is mainly due to vertical wind shear and sedimentation. The contrail gets tilted and stretched in the lateral direction and ice crystals then fall into crystal-free areas below. The level of ambient turbulence is less important for this effect as discussed in Section 3.3.3 and thus a forcing mechanism does not seem to be of primary significance. Similarly, Lewellen et al. (2014) found that "including turbulence regeneration is less important if ... mean wind shear drive more significant levels of turbulent diffusion" (their Section 2.d).

4.2 Contrail identification

Returning thematically to the important question whether microphysical criteria can be found that help to distinguish contrail-cirrus from natural cirrus in observations, the idealised simulations reveals that this is only possible under certain conditions. A contrail core can be identified as an anthropogenic cloud because it has, even after hours, a much higher concentration of ice crystals than natural cirrus formed in-situ if updraught speeds $w_{syn} \gtrsim 10\,\mathrm{cm\,s^{-1}}$ can be ruled out during formation of the latter. Heterogeneous nucleation, which is neglected in our simulations, would make this distinction even clearer since it leads to cirrus with lower ice crystal concentrations than homogeneous nucleation. Typically, a contrail core is also characterised by small crystals (mostly $L < 20\,\mu\mathrm{m}$), much smaller than typical crystals in natural cirrus. Thus, a contrail core can be identified as such in in-situ measurements on the basis of small crystals with very large concentration. Contrail fall streaks cannot be distinguished from natural cirrus in this way, as they consist of much fewer and larger crystals similar to what can be found in cirrus.

Besides such microphysically based approaches, other methods like 1.) chemical identification, 2.) ice crystal residue analysis and 3.) trajectory computations may be helpful.

Aircraft emit chemical species that can be regarded as a passive tracer. Peaks in time series of such in-situ measured species can be attributed to aircraft exhaust plumes. However, ice crystals do sediment in contrast to gaseous exhaust species. Hence, the assumption that the contrail and exhaust plume are collocated is only valid for younger contrails. Using LES simulations, Lewellen et al. (2014, their Figure 4) contrast the dispersion of a contrail and an exhaust plume of a passive tracer. Their findings imply that mainly the cores of aged contrails can be identified with this approach, while their fall streaks are likely to be missed.

So far, analysing ice crystal residues (IR) by mass spectrometry aimed at investigating the chemical composition of aerosols involved in the formation process of natural cirrus clouds (Pratt et al., 2009; Cziczo et al., 2013). This powerful analysis technique may further be used to detect contrails as elemental carbon (EC) has a prominent signature in the mass spectrum. Assuming that nucleation on soot, which consists mainly of EC, exclusively occurs in the cooling aircraft exhaust jets and rarely under natural atmospheric conditions, observed EC IRs give evidence of anthropogenic cloud formation. In-flight operation of mass spectrometers features a high temporal resolution of 5 to 100 Hz. Nevertheless, the actual number of detected IRs is often low (a few ten to hundred IRs for a whole flight leg), as the detection efficiency, in particular of soot, is low (Brands et al., 2011). Hence, the spatial sampling of IRs is too coarse to routinely identify contrails. Moreover, the lower detection limit is 150 nm for IR size, which may not be low enough to safely detect aircraft soot, whose size is roughly 50 nm (Kinsey et al., 2010; Stettler et al., 2013).

Air parcel trajectories can be computed by using NWP model output and flight track data. Considering contrail formation criteria, forward calculations starting from the aircraft position can help to locate the advected contrails (Duda et al., 2004; Schumann, 2012; Schu-

MANN et al., 2013), whereas backward calculations starting from a given contrail position can help to match the contrail to a specific flight (implicitly also determining the contrails' age). SCHUMANN (2012) goes beyond a simple trajectory program, as it includes simplified contrail microphysics, which approximates the effect of sedimentation and the contrail life cycle. Despite this advanced treatment, it is hardly possible to match the advected flight tracks (forward trajectories over a few hours) to specific peaks, e.g. in the lidar backscatter ratio of the observed ice cloud or in-situ sampled tracers. This is due to the fact that the modelled wind fields are too coarse to compute trajectories with sufficient accuracy (SCHUMANN et al., 2013). A rather small error of $2\,\mathrm{m\,s^{-1}}$ in the horizontal wind results in an offset of 40 km in the horizontal position for a 6 hour old contrail. As contrails are rather narrow objects, it turns out that the offset between the real and the computed position is larger than the object's dimension itself. Currently, pure trajectory analyses are not powerful enough to unambiguously match possible contrail observations to specific flights, but they can add a piece of evidence.

The above presented methods rely on different techniques and data sources, which complement each other. Hence, a synergistic use of several such methods (as exemplified in SCHUMANN et al., 2013) may give a strong indication that an observed ice cloud is at least affected by aviation. Nevertheless, distinguishing contrails from cirrus on a local scale, where both cloud types can be strongly intermixed, remains a challenge.

5 Conclusions

The Lagrangian ice microphysical module LCM together with the flow solver EULAG has been used to perform separate simulations of both contrails and cirrus (formed by homogeneous nucleation) in the same idealised environment. For this, scenarios with constant updraught speed (i.e. cooling rates) over a certain time period were used. We fixed the overall adiabatic cooling to 4 K implying that the amount of condensible water vapour is eventually the same in each scenario. This is a standard approach in cirrus and contrail modelling and revealed considerable differences between contrails and cirrus, in terms of their life cycle, size distribution and importance of ambient parameters. The cirrus characteristics are strongly controlled by the updraught speed w_{syn}. The number of ice crystals in the simulated cirrus is proportional to ${w_{syn}}^{1.5}$ confirming analytical estimates, which used simplifying assumptions (KÄRCHER and LOHMANN, 2002). The exponent decreases to 1.2, when stronger turbulent motion is added to the mean ascent. The cirrus lifetime is larger for stronger updraughts, as ice crystals and sedimentation losses are smaller.

Contrail formation and the number of ice crystals generated in a contrail and surviving the vortex phase depends on atmospheric and aircraft parameters (KÄRCHER et al., 2015; LEWELLEN et al., 2014; UNTERSTRASSER, 2014; UNTERSTRASSER, 2016), however it is unaffected by w_{syn}. In strong but short updraughts, ice crystal growth is fast and sedimentation-induced contrail demise sets in quickly. The largest contrail lifetimes occur in slow but enduring updraughts where water vapour becomes continuously available. This may explain the formation of very long living contrails as observed by MINNIS et al. (1998) and LAKEN et al. (2012).

The ice crystal number concentrations n in young contrails and in the contrail core of aged contrails are higher than in most cirrus clouds. In contrail fall streaks, concentrations are substantially smaller than in the core and are similar or smaller than in cirrus. The average n over the complete contrail drops strongly due to contrail dilution and later becomes similar to the values found in cirrus.

Ice crystals of a cirrus are lost due to sedimentation, i.e. the ice crystals fall into the subsaturated layer below and sublimate there. In contrails, the fraction of ice crystal lost by sedimentation is usually smaller than in cirrus. A second type of loss can occur in contrails. Consistent with LEWELLEN (2012) and LEWELLEN et al. (2014), in-situ loss of ice crystals due to spectral ripening occurs, even in slowly ascending air masses. We have not focused on subsidence ($w_{syn} < 0$), which also causes ice crystal loss.

The contrail size distribution (SD) has two distinct peaks, one peak around $L = 20\,\mu\mathrm{m}$, and a second one at $L > 100\,\mu\mathrm{m}$ which depends on the depth of the moist layer. In scenarios with $w_{syn} \lesssim 2\,\mathrm{cm\,s^{-1}}$, spectral ripening occurs and the left tail of the SD reaches down to sizes $L < 1\,\mu\mathrm{m}$. In our set-up the cirrus SDs are narrower than the contrail SDs. However, this result may not be generalised, as we neglected aggregation and more heterogeneous background conditions may also produce broader SDs.

If one can rule out high updraught speeds, observing many small ice crystals indicates the presence of contrails.

In PART 2 (UNTERSTRASSER et al., 2016), simulations of contrails becoming embedded in cirrus are discussed and it is analysed how strongly contrail and cirrus co-exist and impact each other and whether it is meaningful trying to draw a strict separation line between contrails and cirrus.

Acknowledgements

The first author S. UNTERSTRASSER is partly funded by the DFG (German Science Foundation, contract number UN286/1-2). Computational resources were made available by the German Climate Computing Center (DKRZ) through support from the German Federal Ministry of Education and Research (BMBF). The work contributes to the DLR project WeCare. We thank J. SCHNEIDER for discussions on the ice crystal residue technique and U. SCHUMANN for comments on the manuscript.

References

ACP/AMT Special Issue, 2016: ML-CIRRUS – the airborne experiment on natural cirrus and contrail cirrus in mid-latitudes with the high-altitude long-range research aircraft HALO. – http://www.atmos-chem-phys.net/special_issue820.html/.

Baum, B., P. Yang, A. Heymsfield, S. Platnick, M. King, Y.-X. Hu, S. Bedka, 2005: Bulk scattering models for the remote sensing of ice clouds. Part 2: Narrowband models. – J. Appl. Meteor. **44**, 1896–1911.

Brands, M., M. Kamphus, T. Böttger, J. Schneider, F. Drewnick, A. Roth, J. Curtius, C. Voigt, A. Borbon, M. Beekmann, A. Bourdon, T. Perrin, S. Borrmann, 2011: Characterization of a newly developed aircraft-based laser ablation aerosol mass spectrometer (alabama) and first field deployment in urban pollution plumes over paris during megapoli 2009. – Aerosol Sci. Technol. **45**, 46–64, DOI: 10.1080/02786826.2010.517813.

Bugliaro, L., T. Zinner, C. Keil, B. Mayer, R. Hollmann, M. Reuter, W. Thomas, 2011: Validation of cloud property retrievals with simulated satellite radiances: a case study for seviri. – Atmos. Chem. Phys. **11**, 5603–5624, DOI: 10.5194/acp-11-5603-2011.

Burkhardt, U., B. Kärcher, 2009: Process-based simulation of contrail cirrus in a global climate model. – J. Geophys. Res. **114**, D16201, DOI:10.1029/2008JD011491.

Burkhardt, U., B. Kärcher, 2011: Global radiative forcing from contrail cirrus. – Nature Clim. Ch. **1**, 54–58.

Cziczo, D.J., K.D. Froyd, C. Hoose, E.J. Jensen, M. Diao, M.A. Zondlo, J.B. Smith, C.H. Twohy, D.M. Murphy, 2013: Clarifying the dominant sources and mechanisms of cirrus cloud formation. – Science **340**, 1320–1324, DOI: 10.1126/science.1234145.

Diao, M., M.A. Zondlo, A.J. Heymsfield, L.M. Avallone, M.E. Paige, S.P. Beaton, T. Campos, D.C. Rogers, 2014: Cloud-scale ice-supersaturated regions spatially correlate with high water vapor heterogeneities. – Atmos. Chem. Phys. **14**, 2639–2656, DOI:10.5194/acp-14-2639-2014.

Dobbie, S., P. Jonas, 2001: Radiative influences on the structure and lifetime of cirrus clouds. – Quart. J. Roy. Meteor. Soc. **127**, 2663–2682, DOI:10.1002/qj.49712757808.

Duda, D., P. Minnis, L. Nguyen, R. Palikonda, 2004: A case study of the development of contrail clusters over the great lakes. – J. Atmos. Sci. **61**, 1132–1146, DOI: 10.1175/1520-0469(2004)061<1132:ACSOTD>2.0.CO;2.

Duda, D.P., R. Palikonda, P. Minnis, 2009: Relating observations of contrail persistence to numerical weather analysis output. – Atmos. Chem. Phys. **9**, 1357–1364, DOI: 10.5194/acp-9-1357-2009.

Febvre, G., J.-F. Gayet, A. Minikin, H. Schlager, V. Shcherbakov, O. Jourdan, R. Busen, M. Fiebig, B. Kärcher, U. Schumann, 2009: On optical and microphysical characteristics of contrails and cirrus. – J. Geophys. Res. **114**, D02204.

Forster, L., C. Emde, S. Unterstrasser, B. Mayer, 2012: Effects of three-dimensional photon transport on the radiative forcing of realistic contrails. – J. Atmos. Sci. **69**, 2243–2255, DOI:10.1175/JAS-D-11-0206.1.

Freudenthaler, V., F. Homburg, H. Jäger, 1995: Contrail observations by ground-based scanning lidar: Cross-sectional growth. – Geophys. Res. Lett. **22**, 3501–3504.

Gao, R., P. Popp, D. Fahey, T. Marcy, R. Herman, E. Weinstock, D. Baumgardner, T. Garrett, K. Rosenlof, T. Thompson, others, 2004: Evidence that nitric acid increases relative humidity in low-temperature cirrus clouds. – Science **303**, 516–520.

Gierens, K., 1998: How the Sky Gets Covered with Condensation Trails. – Meteorol. Z. **7**, 181–187.

Gierens, K., 2003: On the transition between heterogeneous and homogeneous freezing. – Atmos. Chem. Phys. **3**, 437–446.

Gierens, K., S. Bretl, 2009: Analytical treatment of ice sublimation and test of sublimation parameterisations in two-moment ice microphysics models. – Atmos. Chem. Phys. **9**, 7481–7490.

Haag, W., B. Kärcher, J. Ström, A. Minikin, U. Lohmann, J. Ovarlez, A. Stohl, 2003: Freezing thresholds and cirrus cloud formation mechanisms inferred from in situ measurements of relative humidity. – Atmos. Chem. Phys. **3**, 1791–1806.

Haywood, J.M., R.P. Allan, J. Bornemann, P.M. Forster, P.N. Francis, S. Milton, G. Rädel, A. Rap, K.P. Shine, R. Thorpe, 2009: A case study of the radiative forcing of persistent contrails evolving into contrail-induced cirrus. – J. Geophys. Res. **114**, D24201.

Heymsfield, A., R. Lawson, G. Sachse, 1998: Growth of ice crystals in a precipitating contrail. – Geophys. Res. Lett. **25**, 1335–1338.

Ivanova, D., D.L. Mitchell, W.P. Arnott, M. Poellot, 2001: A GCM parameterization for bimodal size spectra and ice mass removal rates in mid-latitude cirrus clouds. – Atmos. Res. **59**, 89–113, DOI:10.1016/S0169-8095(01)00111-9.

Iwabuchi, H., P. Yang, K. Liou, P. Minnis, 2012: Physical and optical properties of persistent contrails: Climatology and interpretation. – J. Geophys. Res. **117**, D06215.

Jensen, E., A. Ackerman, D. Stevens, O. Toon, P. Minnis, 1998: Spreading and growth of contrails in a sheared environment. – J. Geophys. Res. **103**, 31557–31568.

Jensen, E.J., L. Pfister, O.B. Toon, 2011: Impact of radiative heating, wind shear, temperature variability, and microphysical processes on the structure and evolution of thin cirrus in the tropical tropopause layer. – J. Geophys. Res. **116**, D12209, DOI:10.1029/2010JD015417.

Kärcher, B., U. Lohmann, 2002: A parameterization of cirrus cloud formation: Homogeneous freezing of supercooled aerosols. – J. Geophys. Res. **107**, 4010.

Kärcher, B., F. Yu, 2009: Role of aircraft soot emissions in contrail formation. – Geophys. Res. Lett. **36**, L01804, DOI: 10.1029/2008GL036649.

Kärcher, B., R. Busen, A. Petzold, F.P. Schröder, U. Schumann, E.J. Jensen, 1998: Physicochemistry of aircraft-generated liquid aerosols, soot, and ice particles. 2. Comparison with observations and sensitivity studies. – J. Geophys. Res. **103**, 17129–17148.

Kärcher, B., J. Hendricks, U. Lohmann, 2006: Physically based parameterization of cirrus cloud formation for use in global atmospheric models. – J. Geophys. Res. **111**, D01205. DOI:10.1029/2005JD006219

Kärcher, B., U. Burkhardt, S. Unterstrasser, P. Minnis, 2009: Factors controlling contrail cirrus optical depth. – Atmos. Chem. Phys. **9**, 6229–6254.

Kärcher, B., A. Dörnbrack, I. Sölch, 2014: Supersaturation variability and cirrus ice crystal size distributions. – J. Atmos. Sci. **71**, 2905–2926, DOI:10.1175/JAS-D-13-0404.1.

Kärcher, B., U. Burkhardt, A. Bier, L. Bock, I.J. Ford, 2015: The microphysical pathway to contrail formation. – J. Geophys. Res. **120**, 7893–7927, DOI: 10.1002/2015JD023491.

Kaufmann, S., C. Voigt, P. Jessberger, T. Jurkat, H. Schlager, A. Schwarzenboeck, M. Klingebiel, T. Thornberry, 2014: In situ measurements of ice saturation in young contrails. – Geophys. Res. Lett. **41**, 702–709, DOI: 10.1002/2013GL058276.

Khvorostyanov, V.I., K. Sassen, 1998: Cirrus cloud simulation using explicit microphysics and radiation. part ii: Microphysics, vapor and ice mass budgets, and optical and radiative properties. – J. Atmos. Sci. **55**, 1822–1845, DOI: 10.1175/1520-0469(1998)055<1822:CCSUEM>2.0.CO;2.

Kinsey, J., Y. Dong, D. Williams, R. Logan, 2010: Physical characterization of the fine particle emissions from commercial aircraft engines during the aircraft particle emissions experiment (apex) 1-3. – Atmos. Environ. **44**, 2147–2156, DOI: 10.1016/j.atmosenv.2010.02.010.

Krämer, M., C. Schiller, A. Afchine, R. Bauer, I. Gensch, A. Mangold, S. Schlicht, N. Spelten, N. Sitnikov, S. Borrmann, M. de Reus, P. Spichtinger, 2009: Ice supersaturations and cirrus cloud crystal numbers. – Atmos. Chem. Phys. **9**, 3505–3522, DOI:10.5194/acp-9-3505-2009.

Lainer, M., 2012: Numerische Simulationen von langlebigen Kondensstreifen mit Lagrange'scher Mikrophysik (in German). – Master's thesis, LMU München, Meteorologie, http://elib.dlr.de/81136/.

Laken, B.A., E. Pallé, D.R. Kniveton, C.J.R. Williams, D.A. Kilham, 2012: Contrails developed under frontal influences of the north atlantic0. – J. Geophys. Res. **117**, D11201.

Lawson, R., A. Heymsfield, S. Aulenbach, T. Jensen, 1998: Shapes, sizes and light scattering properties of ice crystals in cirrus and a persistent contrail during SUCCESS. – Geophys. Res. Lett. **25**, 1331–1334.

Lewellen, D.C., 2012: Analytic solutions for evolving size distributions of spherical crystals or droplets undergoing diffusional growth in different regimes.. – J. Atmos. Sci. **69**, 417–434.

Lewellen, D.C., 2014: Persistent contrails and contrail cirrus. Part 2: Full Lifetime Behavior. – J. Atmos. Sci., published online, 4420–4438, DOI:10.1175/JAS-D-13-0317.1.

Lewellen, D.C., O. Meza, W.W. Huebsch, 2014: Persistent contrails and contrail cirrus. Part 1: Large-eddy simulations from inception to demise. – J. Atmos. Sci., published online, 4399–4419, DOI:10.1175/JAS-D-13-0316.1.

Liu, H., P. Wang, R. Schlesinger, 2003: A Numerical Study of Cirrus Clouds. Part II: Effects of Ambient Temperature, Stability, Radiation, Ice Microphysics, and Microdynamics on Cirrus Evolution. – J. Atmos. Sci. **60**, 1097–1119.

Luebke, A., L. Avallone, C. Schiller, J. Meyer, C. Rolf, M. Krämer, 2013: Ice water content of arctic, midlatitude, and tropical cirrus – part 2: Extension of the database and new statistical analysis. – Atmos. Chem. Phys. **13**, 6447–6459.

McFarquhar, G.M., A.J. Heymsfield, 1998: The definition and significance of an effective radius for ice clouds. – J. Atmos. Sci. **55**, 2039–2052.

Milbrandt, J., R. McTaggart-Cowan, 2010: Sedimentation-induced errors in bulk microphysics schemes. – J. Atmos. Sci. **67**, 3931–3948, DOI:10.1175/2010JAS3541.1.

Minnis, P., D. Young, D. Garber, L. Nguyen, W. Smith Jr, R. Palikonda, 1998: Transformation of contrails into cirrus during SUCCESS. – Geophys. Res. Lett. **25**, 1157–1160.

Mitchell, D., 1996: Use of mass- and area-dimensional power laws for determining precipitation particle terminal velocities. – J. Atmos. Sci. **53**, 1710–1723.

Mitchell, D.L., 2002: Effective diameter in radiation transfer: General definition, applications, and limitations. – J. Atmos. Sci. **59**, 2330–2346.

Mitchell, D.L., S.K. Chai, Y. Liu, A.J. Heymsfield, Y. Dong, 1996: Modeling Cirrus Clouds. Part I: Treatment of Bimodal Size Spectra and Case Study Analysis. – J. Atmos. Sci. **53**, 2952–2966, DOI: 10.1175/1520-0469(1996)053<2952:MCCPIT>2.0.CO;2.

Nakajima, T., M.D. King, 1990: Determination of the optical thickness and effective particle radius of clouds from reflected solar radiation measurements. part i: Theory. – J. Atmos. Sci. **47**, 1878–1893, DOI: 10.1175/1520-0469(1990)047<1878:DOTOTA>2.0.CO;2.

Ovarlez, J., J.-F. Gayet, K. Gierens, J. Ström, H. Ovarlez, F. Auriol, R. Busen, U. Schumann, 2002: Water vapour measurements inside cirrus clouds in northern and southern hemispheres during inca. – Geophys. Res. Lett. **29**, 1813, DOI: 10.1029/2001GL014440.

Platnick, S., 2000: Vertical photon transport in cloud remote sensing problems. – J. Geophys. Res. **105**, 22919–22935, DOI:10.1029/2000JD900333.

Poellot, M.R., W.P. Arnott, J. Hallett, 1999: In situ observations of contrail microphysics and implications for their radiative impact. – J. Geophys. Res. **104**, 12077–12084, DOI: 10.1029/1999JD900109.

Ponater, M., S. Marquart, R. Sausen, 2002: Contrails in a comprehensive global climate model: Parameterization and radiative forcing results. – J. Geophys. Res. **107**, 941–960.

Pratt, K.A., P.J. DeMott, J.R. French, Z. Wang, D.L. Westphal, A.J. Heymsfield, C.H. Twohy, A.J. Prenni, K.A. Prather, 2009: In situ detection of biological particles in cloud ice-crystals. – Nature Geosci. **2**, 398–401.

Rap, A., P. Forster, A. Jones, O. Boucher, J. Haywood, N. Bellouin, R. De Leon, 2010: Parameterization of contrails in the UK Met Office Climate Model. – J. Geophys. Res. **115**, D10205, DOI:10.1029/2009JD012443.

Schröder, F., B. Kärcher, C. Duroure, J. Ström, A. Petzold, J. Gayet, B. Strauss, P. Wendling, S. Borrmann, 2000: On the Transition of Contrails into Cirrus Clouds. – J. Atmos. Sci. **57**, 464–480.

Schumann, U., 1996: On conditions for contrail formation from aircraft exhausts. – Meteorol. Z. **5**, 4–23.

Schumann, U., 2012: A contrail cirrus prediction model. – Geosci. Model Dev. **5**, 543–580, DOI: 10.5194/gmd-5-543-2012.

Schumann, U., K. Graf, 2013: Aviation-induced cirrus and radiation changes at diurnal timescales. – J. Geophys. Res. 118, 2404–2421, DOI:10.1002/jgrd.50184.

Schumann, U., H. Schlager, F. Arnold, R. Baumann, P. Haschberger, O. Klemm, 1998: Dilution of aircraft exhaust plumes at cruise altitudes. – Atmos. Environ. **32**, 3097–3103.

Schumann, U., B. Mayer, K. Gierens, S. Unterstrasser, P. Jessberger, A. Petzold, C. Voigt, J.-F. Gayet, 2011: Effective radius of ice particles in cirrus and contrails. – J. Atmos. Sci. **68**, 300–321, DOI:10.1175/2010JAS3562.1.

Schumann, U., R. Hempel, H. Flentje, M. Garhammer, K. Graf, S. Kox, H. Lösslein, B. Mayer, 2013: Contrail study with ground-based cameras. – Atmos. Meas. Tech. **6**, 3597–3612, DOI:10.5194/amt-6-3597-2013.

Smolarkiewicz, P., L. Margolin, 1997: On Forward-in-Time Differencing for Fluids: an Eulerian/Semi-Lagrangian Non-Hydrostatic Model for Stratified Flows. – In: C. Lin, R. Laprise, H. Ritchie (Eds.): Numerical Methods in Atmospheric and Oceanic Modelling: The André J. Robert Memorial Volume **35**. – Canadian Meteorological and Oceanographical Society, Ottawa, Canada, 127–152.

Smolarkiewicz, P., L. Margolin, 1998: MPDATA: A Finite-Difference Solver for Geophysical Flows. – J. Comput. Phys. **140**, 459–480.

Sölch, I., B. Kärcher, 2010: A large-eddy model for cirrus clouds with explicit aerosol and ice microphysics and Lagrangian ice particle tracking. – Quart. J. Roy. Meteor. Soc. **136**, 2074–2093.

Sölch, I., B. Kärcher, 2011: Process-oriented large-eddy simulations of a midlatitude cirrus cloud system based on observations. – Quart. J. Roy. Meteor. Soc. **137**, 374–393.

Spichtinger, P., K. Gierens, 2009a: Modelling of cirrus clouds – Part 2: Competition of different nucleation mechanisms. – Atmos. Chem. Phys. **9**, 2319–2334.

Spichtinger, P., K.M. Gierens, 2009b: Modelling of cirrus clouds –Part 1b: Structuring cirrus clouds by dynamics. – Atmos. Chem. Phys. **9**, 707–719.

Spichtinger, P., K. Gierens, H. Smit, J. Ovarlez, J. Gayet, 2004: On the distribution of relative humidity in cirrus clouds. – Atmos. Chem. Phys. **4**, 639–647.

Stettler, M., J. Swanson, S. Barrett, A. Boies, 2013: Updated correlation between aircraft smoke number and black carbon concentration. – Aerosol Sci. Technol. **47**, 1205–1214, DOI:10.1080/02786826.2013.829908.

Ström, J., S. Ohlsson, 1998: In situ measurements of enhanced crystal number densities in cirrus clouds caused by aircraft exhaust. – J. Geophys. Res. **103**, 11355–11361.

Sussmann, R., K. Gierens, 1999: Lidar and numerical studies on the different evolution of vortex pair and secondary wake in young contrails. – J. Geophys. Res. **104**, 2131–2142.

Unterstrasser, S., 2014: Large eddy simulation study of contrail microphysics and geometry during the vortex phase and consequences on contrail-to-cirrus transition. – J. Geophys. Res. **119**, 7537–7555, DOI:10.1002/2013JD021418.

Unterstrasser, S., 2016: Properties of young contrails – a parametrisation based on large-eddy simulations. – Atmos. Chem. Phys. **16**, 2059–2082, DOI: 10.5194/acp-16-2059-2016.

Unterstrasser, S., K. Gierens, 2010a: Numerical simulations of contrail-to-cirrus transition – Part 1: An extensive parametric study. – Atmos. Chem. Phys. **10**, 2017–2036.

Unterstrasser, S., K. Gierens, 2010b: Numerical simulations of contrail-to-cirrus transition – Part 2: Impact of initial ice crystal number, radiation, stratification, secondary nucleation and layer depth. – Atmos. Chem. Phys. **10**, 2037–2051.

Unterstrasser, S., N. Görsch, 2014: Aircraft-type dependency of contrail evolution. – J. Geophys. Res. **119**, 14,015–14,027, DOI:10.1002/2014JD022642.

Unterstrasser, S., I. Sölch, 2013: Numerical Modeling of contrail cluster formation. – In: Sausen, R., S. Unterstrasser, A. Blum (Eds.): Proceedings of the 3rd International Conference on Transport, Atmosphere and Climate, 25.-28. Juni 2012, Prien, Deutschland, 114–119.

Unterstrasser, S., I. Sölch, 2014: Optimisation of simulation particle number in a Lagrangian ice microphysical model. – Geosci. Model Dev. **7**, 695–709, DOI: 10.5194/gmd-7-695-2014.

Unterstrasser, S., R. Paoli, I. Sölch, C. Kühnlein, T. Gerz, 2014: Dimension of aircraft exhaust plumes at cruise conditions: effect of wake vortices. – Atmos. Chem. Phys. **14**, 2713–2733, DOI:10.5194/acp-14-2713-2014.

Unterstrasser, S., K. Gierens, I. Sölch, M. Wirth, 2016: Numerical simulations of homogeneously nucleated natural cirrus and contrail-cirrus. Part 2: Interaction on local scale – Meteorol. Z., DOI:10.1127/metz/2016/0780.

van de Hulst, H.C., 1981: Light scattering by small particles. – Dover.

Wacker, U., A. Seifert, 2001: Evolution of rain water profiles resulting from pure sedimentation: Spectral vs. parameterized description. – Atmos. Res. **58**, 19–39.

Yang, P., K. Liou, K. Wyser, D. Mitchell, 2000: Parameterization of the scattering and absorption properties of individual ice crystals. – J. Geophys. Res. **105**, 4699–4718.